Analytical and Numerical Investigation of a Small-scale Radial-Inflow Steam Turbine

ÉCOLE POLYTECHNIQUE FÉDÉRALE DE LAUSANNE
SCHOOL OF ENGINEERING
INSTITUTE OF MECHANICAL ENGINEERING
LABORATORY FOR APPLIED MECHANICAL DESIGN

Author:

Marcos Font Armenteras

Supervisors:

Professor J. Schiffmann

P. H. Wagner

Lausanne, Switzerland

January 2019

ABSTRACT

This thesis compares experiments to the analytical and numerical investigation of a small-scale radial-inflow turbine (diameter of 15 mm). This turbine is part of the Fan-Turbine Unit (FTU). The turbine of this FTU propels the fan that recirculates the unused hydrogen and water vapor from the anode off-gas of a Solid Oxide Fuel Cell (SOFC) to its inlet. This recirculation improves the electrical efficiency of the SOFC system due to higher global fuel utilization and allows for an operation without external water supply for the steam reformer. Due to its high efficiencies, also at small-scale and the possibility for heat cogeneration, it is competitive compared with other energy generation systems.

The main objective of this thesis is to improve the existing analytical and numerical models of the turbine and compare their respective results with experimental measurements. Good results are obtained with the analytical (38 Watt) and the numerical investigation (43 Watt), if the gas film bearing mechanical loss (18 Watt) is added to the experimental measurement (22 Watt). The turbine power at the design point is very low (40 Watt) compared to the bearing mechanical losses (18 Watt), so heat fluxes to the turbine impeller domain have a high impact.

CONTENTS

LIST OF FIGURES

LIST OF TABLES

NOMENCLATURE

GREEK SYMBOLS

α	Absolute velocity angle	rad
β	Relative velocity angle	rad
η	Efficiency	-
ε	Absolute roughness	mm
ϵ_a	Admission ratio	-
f_D	Friction coefficient	-
μ	Dynamic viscosity	Pa·s
δ	Degree of reaction	-
ρ	Density	kg/m^3
ω	Angular velocity	rad/s

ROMAN SYMBOLS

A	Area	m^2
b	Channel width	m
c	Absolute velocity	m/s
c_s	Sound velocity	m/s
C_u	Transversal absolute velocity	m/s
C_m	Meridional absolute velocity	m/s
C_p	Heat capacity at constant pressure	J/K
C	Courant number	-
D	Diameter	m
d	Distance between blades	m
h	Blade height	m
h	Specific enthalpy	J/kg
k	Heat capacity ratio	-

L	Length	m
$\dot{m}$	Mass flow rate	kg/s
Ma	Mach number	-
P	Power	W
p	Pressure	Pa
r	Radius	m
R	Universal gas constant	J/K·mol
Ra	Mean roughness	mm
Re	Reynolds number	-
T	Temperature	K
t	Time	s
u	Circumferential velocity	m/s
w	Relative velocity	m/s
W_u	Transversal relative velocity	m/s
W_m	Meridional relative velocity	m/s
x	Length	m

1 INTRODUCTION

This chapter outlines the main motivations of this thesis and gives an overview of the thesis with a short description of the context and objectives.

1.1 MOTIVATIONS

The world's energy consumption is increasing in a fast way. This is the reason why it is important to find new solutions to generate this energy. These solutions have to satisfy two important objectives. Firstly, they have to generate energy in a long-term basis. Secondly, the generating method of this energy should try to solve the environmental problem all around the world.

The efficiency of the Solid Oxide Fuel Cell (SOFC) system is one of the bests in terms of energy generation and compared with the rest of electricity generation methods based on fossil fuels. This high efficiency is reached because the energy is obtained directly from a chemical reaction and because the main process does not involve mechanical interaction and thus losses are avoided. However, the hydrogen conversion rate within the SOFC stack is limited and there is part of the hydrogen that is not oxidized in the stack. A Fan Turbine Unit (FTU) allows for the recirculation of the anode off-gas and thus it increases the efficiency due to higher hydrogen utilization. Additionally, the water vapor that is contained in the anode off-gas can be used for the steam reforming of the methane at the reformer. This reformer is located at the anode inlet and reforms the natural gas to hydrogen. The micro-fan used to recirculate the fluid is propelled by a small-scale turbine. This small-scale turbine is the one studied in this thesis.

1.2 CONTEXT AND OBJECTIVES

The fan-turbine unit (FTU) used to recirculate the anode off-gas of a 10 kWe SOFC system was designed, optimized and tested by Wagner [1]. This turbine is a small-scaled turbine with a 15 mm diameter and propels a micro-fan with a diameter of 19 mm. Wagner [1] used the commercial software ANSYS CFX to design the three-dimensional shape of the turbine.

Figure 1.1 shows a schematic of the radial-inflow partial-admission turbine and the nomenclature of the different sections and important components. The turbine consists basically of three main parts: the turbine inlet (1 to 5), the turbine rotor and stator (5 to 8) and the turbine outlet (8 to 12).

The existing numerical model for this turbine was made from the inducer inlet (section 4) to the exducer outlet (section 9) (Figure 1.1) and it does not consider the fluid losses within the inlet and the outlet pipes. Although the losses in these pipes are very low, this thesis calculates these losses to make

the calculations more accurate. This allows for a more accurate comparison of the analytical and numerical models, as well as the experimental measurements done by Wagner [1].

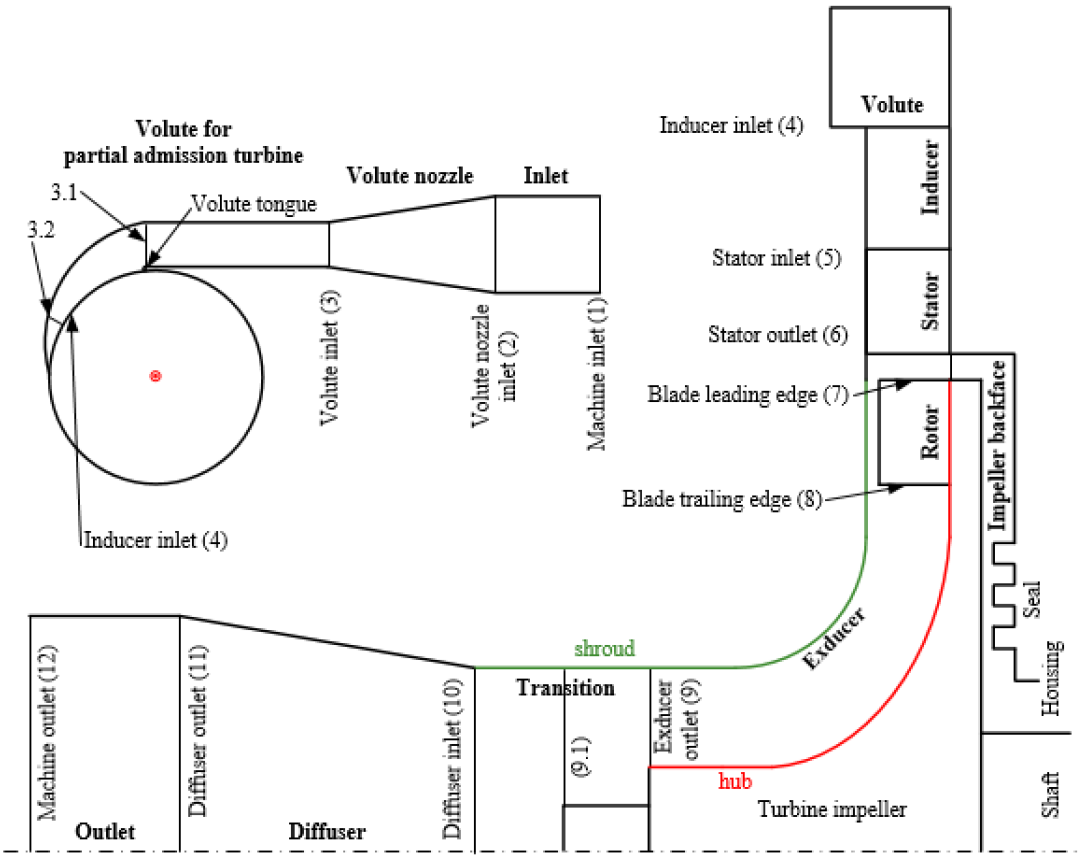

Figure 1.1 - Meridional view of a schematic partial-admission radial-inflow turbine, as well as the nomenclature of the different sections and important components. Adapted from [1]

For this reason, an analytical and a numerical model are made to calculate these losses. After being compared and validated, these models allow for a more accurate specification of the boundary conditions for both the analytical and numerical models.

The turbine numerical model is adapted and the boundary conditions are modified in order to get more accurate results and an improved numerical model for the real turbine.

The main objectives of this thesis are:

- To calculate the pressure losses at the inlet and at the outlet pipes of the radial-inflow turbine, as well as the volute outlet velocity angle (inlet and outlet boundary adaptation)
- To perform analytical and numerical models to verify and automatize these calculations

- To improve the existing numerical computational fluid dynamics simulation with the commercial software Ansys CFX
- Analise the experimental results of the radial-inflow turbine and compare these results to the analytical and numerical models
- Evaluate the results critically and suggest improvements towards the analytical model and the numerical simulation.

2 THEORY

This chapter gives a general overview of the SOFC system and the turbine studied in this thesis.

2.1 SOLID OXIDE FUEL CELL SYSTEM

Figure 2.1 shows several stationary SOFC systems with a schematic SOFC cell. Although the cathode off-gas could also be recirculated, Figure 2.1 shows only the anode off-gas recirculation (AOR) subsystems. The anode off-gas recirculation is advantageous as it can increase the global fuel utilization (FU). A high FU is beneficial for a system with high electrical power output, respectively high electrical efficiencies. The AOR can increase the global FU without increasing the local FU and thus increase the system electrical efficiency without compromising the SOFC stack lifetime. Another advantage of the AOR is the reutilization of the water vapor in the anode exhaust. This water vapor is already deionized and non-corrosive, as the water vapor is not condensed. Thus, this water vapor can be used directly for the steam reformer at the anode inlet [1].

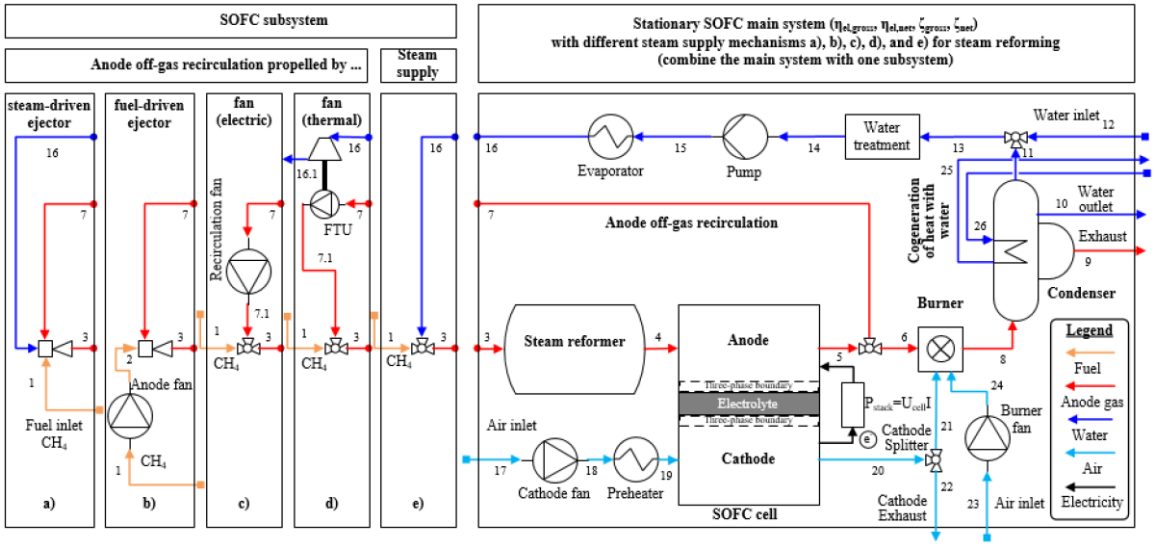

Figure 2.1 – Stationary SOFC systems with steam reformer, schematic SOFC cell, burner, condenser, evaporator and anode off-gas recirculation propelled by a) a steam-driven ejector, b) a fuel-driven ejector, c) an electrically-driven fan, d) a patented thermally-driven fan, as well as e) direct steam supply for the steam reforming. [1]

2.2 TURBINE

This thesis is focused on the turbine of the FTU. Figure 1.1 shows a schematic of this radial-inflow partial-admission turbine.

A turbine receives a fluid with high pressure and expands it to low pressure converting the fluid's mechanical energy to mechanical energy in the shaft. The basic element of the turbine is the rotor, where it has the blades distributed all around the circumference. Upstream of the turbine rotor, a stator is located that accelerates and turns the flow. This stator gives a pre-swirl to the fluid to minimize the total to total specific enthalpy difference over the turbine impeller, and consequently maximize the turbine power output. The turbine studied in this thesis is a radial-inflow partial-admission turbine and this is the reason why the stator does not have its blades all around the circumference. This turbine has an admission of 13 blades out of 61 (≈ 21 %).

The specific enthalpy difference of the turbine (Δh_{tt}) is equal to the Euler equation when neglecting the shroud torque

$$\Delta h_{tt} = c_{u,8} \cdot u_8 - c_{u,7} \cdot u_7 \tag{2.1}$$

where c_u is the transversal component of the fluid absolute velocity and u is the circumferential velocity of the blade (shown and explained in Figure 3.2). The turbine Leading Edge (LE) is at section 7, whereas the Trailing Edge (TE) is at plane 8 (see Figure 1.1).

Assuming a stationary adiabatic system, the turbine power can be calculated with the first law of thermodynamics

$$P_{turbine} = \dot{m}_8 \cdot h_{t,8} - \dot{m}_7 \cdot h_{t,7} \approx \dot{m}_8 \cdot (h_{t,8} - h_{t,7}) \tag{2.2}$$

This definition of the turbine power is used to calculate the isentropic total to total efficiency of the rotor

$$\eta_{is,rotor} = \frac{h_{t,8} - h_{t,7}}{h_{t,is,8} - h_{t,7}} \tag{2.3}$$

The total to total isentropic efficiency of the whole turbine can be defined as

$$\eta_{is,turbine} = \frac{h_{t,8} - h_{t,5}}{h_{t,is,8} - h_{t,5}} \tag{2.4}$$

The stator LE is at plane 5, whereas the TE is at plane 6 (see Figure 1.1).

The specific enthalpy difference can also be calculated with the temperature difference and the heat capacity at constant pressure (C_p)

$$\Delta h_{tt} = C_p \cdot (T_7 - T_8) \tag{2.5}$$

Thus, the turbine power can also be expressed as

$$P_{turbine} = \dot{m}_8 \cdot C_p \cdot (T_7 - T_8) \tag{2.6}$$

The degree of reaction is a non-dimensional number used for the turbine design.

$$\delta_h = \frac{\Delta h_{rotor}}{\Delta h_{stage}} \tag{2.7}$$

The degree of reaction is the fraction of the rotor specific enthalpy difference to the stage (rotor and stator) specific enthalpy difference. This reaction is always between 0 and 1, whereas turbines with a reaction of 0 or 1 are not achievable since there are always some frictional pressure losses within the rotor and the stator. Turbines with higher efficiencies are built at a degree of reaction of 0,5 [2]. Due to the high static pressure between the rotor and stator, a high reaction turbine is not capable for a partial-admission operation. The power density of a low reaction turbine is higher (about twice as much as a 0,5-reaction turbine with a similar mass flow rate). The α_8 and β_7 are more favorable, respectively the change of direction of the absolute velocity is higher. A higher change of velocity also involves higher aerodynamic losses; hence the low-reaction turbines have an inferior efficiency. Additionally, losses occur due to the increased velocities which are higher at the stator outlet, respectively at the rotor inlet compared to the 0,5 reaction turbines.

3 ANALYTICAL CALCULATIONS

This chapter shows the analytical calculations made for the turbine power and efficiency, as well as the inlet and outlet pressure losses and the volute outlet velocity angle.

3.1 TURBINE POWER AND EFFICIENCY

In this section, the turbine power is calculated with the two possible methods: (1) with the Euler equation (3.1) and the design parameters of the turbine and (2) with the first law of thermodynamics according to equation (2.6). The boundary conditions for the analytical calculations shown in this section are at the design point of the turbine (168 krpm).

To calculate the turbine power with the Euler equation (3.1) it is necessary to calculate the velocity triangles of the turbine rotor

$$P_{turbine} = \dot{m}_8 \cdot \Delta h_{tt} = \dot{m}_8 \cdot (c_{u,8} \cdot u_8 - c_{u,7} \cdot u_7) \tag{3.1}$$

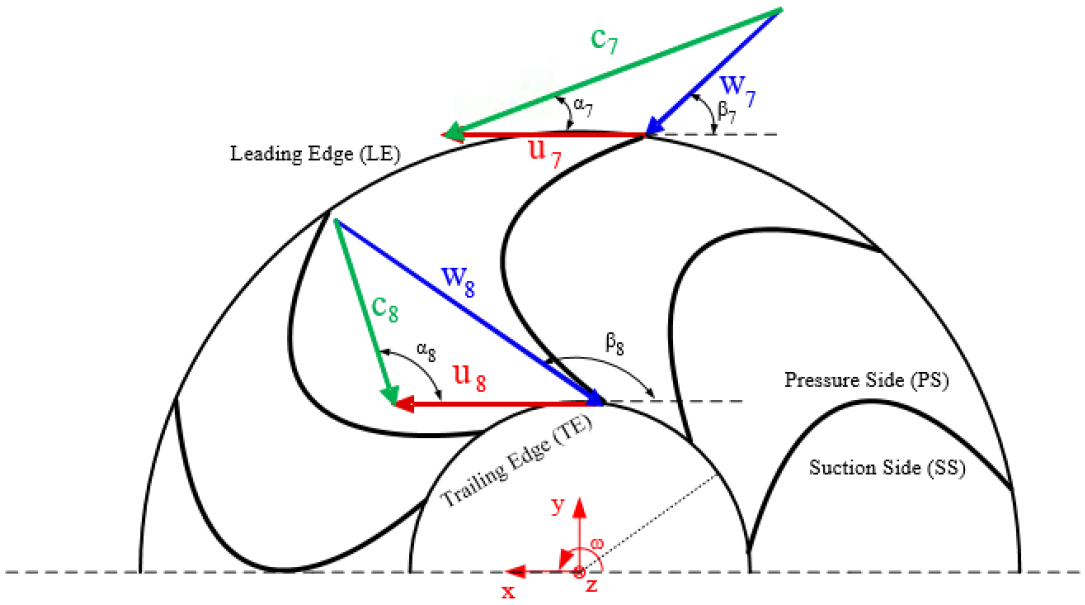

Figure 3.1 - Top view of a schematic turbine and the velocity triangles at the leading and trailing edge

The colour triangles (Figure 3.1) formed by the velocity vectors "u", "c" and "w" explain how a turbine works and are used to calculate the turbine power with the Euler equation. The "u" vectors are the circumferential velocities of the blade, the "c" vectors are the absolute velocities of the fluid and the

"w" vectors are the relative velocities of the fluid with respect to the rotating blades. The absolute velocity is equal to the relative velocity plus the blade's circumferential velocity. The inlet part of the rotor is the Leading Edge (7) and the outlet is the Trailing Edge (8).

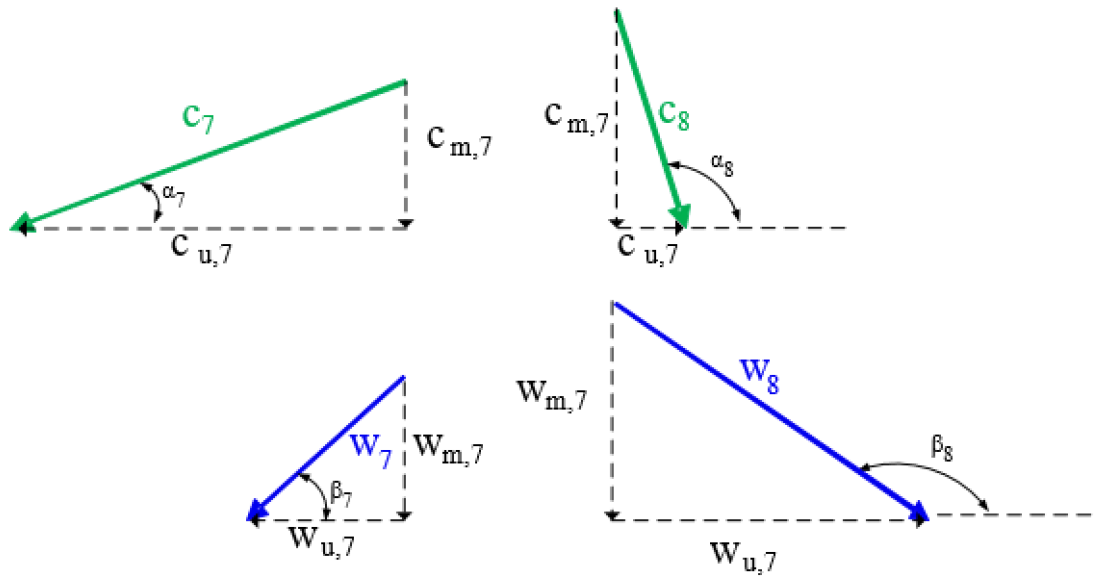

Figure 3.2 – Breakdown of the velocity vectors into the meridional (c_m and w_m) and transversal (c_u and w_u) components at the LE (section 7) and TE (section 8) of the rotor

The boundary conditions needed to calculate this power analytically are the inlet and the outlet total pressures of the fluid, the inlet and the outlet total temperatures and the mass flow rate.

Since the pressure ratio of the turbine (2,8) is higher than the critical pressure ratio (1,9), the Mach number in the critical section can be assumed equal to 1. This critical section is at the stator outlet, where the fluid velocity is equal to the sound velocity. The sound velocity (c_s) is defined by the following equation (3.2)

$$c_s = \sqrt{K \cdot R \cdot T} \tag{3.2}$$

Then, considering the inlet volute adiabatic and using the temperature at the inlet, the sound speed at the stator TE is 445 m/s. Thus, the fluid velocity at section 6 (c_6) is also 445 m/s.

Table 3.1 - Geometrical parameters of the turbine needed for the analytical calculations

Parameter	**Nomenclature**	**Value**
TE stator blade angle at section 6	α_6	$0{,}38\ rad$
LE rotor blade angle at section 7	β_7	$0{,}64\ rad$
Radius at section 7	r_7	$7{,}5 \cdot 10^{-3}\ m$
TE rotor blade angle at section 8	β_8	$2{,}41\ rad$
Radius at section 8	r_8	$6{,}5 \cdot 10^{-3}\ m$
Distance between blades	d_8	$0{,}695\ mm$
Height of the blades	h_8	$0{,}586\ mm$
Area between blades	A_8	$5{,}3\ mm^2$
Rotational speed of the rotor	ω	$17.614\ rad/s$

As shown in Figure 3.1 α is the angle between the absolute velocity and the circumferential velocity of the blade and β is the angle between the relative velocity and the circumferential velocity of the blade.

The components of the velocity triangle (Figure 3.1 and Figure 3.2) are calculated with the geometry parameters shown in Table 3.1.

$$c_{u,6} = c_6 \cdot \cos(\alpha_6) = 411{,}5\ m/s \tag{3.3}$$

$$c_{u,7} = \frac{c_{u,6} \cdot r_6}{r_7} = 419{,}7\ m/s \tag{3.4}$$

$$u_7 = \omega \cdot r_7 = 132{,}1\ m/s \tag{3.5}$$

$$c_{m,8} = \frac{\dot{m}}{3600 \cdot \rho \cdot A_8 \cdot 10^{-6}} = 162{,}9\ m/s \tag{3.6}$$

$$w_8 = \frac{c_{m,8}}{\sin(\pi - \beta_8)} = 244{,}4\ m/s \tag{3.7}$$

$$w_{u,8} = w_8 \cdot \cos(\pi - \beta_8) = 182{,}2\ m/s \tag{3.8}$$

$$u_8 = w \cdot r_8 = 114{,}5\ m/s \tag{3.9}$$

$$c_{u,8} = w_{u,8} - u_8 = 67{,}7\ m/s \tag{3.10}$$

With all the velocity components known it is possible to calculate the turbine power with the Euler equation

$$P_{turbine} = \dot{m} \cdot \left(c_{u,7} \cdot u_7 - c_{u,8} \cdot u_8\right) = 37{,}9\ W \tag{3.11}$$

This turbine power can also be calculated with the heat capacity at constant pressure and the decrease of temperatures

$$P_{turbine} = \dot{m} \cdot C_p \cdot \Delta T = 21{,}9\ W \tag{3.12}$$

This power is calculated with the measured temperature difference between the inlet (section 1 in Figure 1.1) and the outlet (section 12) of the turbine. The difference between both methods (16 W) is caused by the difference between the temperature at the outlet of the turbine (section 12) and at the outlet of the turbine rotor (section 8). Between the rotor outlet and the turbine outlet, a heat flux due to the bearing mechanical losses crosses the turbine fluid domain and thus the turbine outlet temperature is increased. This is the main reason of the difference between both methods for the power calculation. This heat flux coming from the bearings was measured and calculated by Wagner [1] and it is around 18 W. Then, assuming that this heat flux crosses the turbine, the adjusted turbine power is 39,9 W. With this corrected power the corrected total temperature at the rotor outlet is calculated as (3.13)

$$T_{out,corrected} = T_{in} - \frac{P_{corrected}}{\dot{m} \cdot C_p} \tag{3.13}$$

This corrected total temperature at the outlet is 171 ºC. The efficiency of the turbine is then calculated with this corrected temperature.

$$\eta_{is,turbine} = \frac{h_{t,8} - h_{t,5}}{h_{t,is,8} - h_{t,5}} = \frac{(T_{t,in} - T_{t,out,corrected})}{T_{t,in} \cdot \left(1 - \left(\frac{P_{s,out}}{P_{t,in}}\right)^{\frac{k-1}{k}}\right)} \tag{3.14}$$

The results of the isentropic efficiency with the corrected outlet temperature is 43,6 %, whereas with the non-corrected temperature it is 24 % (with the measured outlet temperature of 193,1 ºC).

The Matlab scripts performed to automatize these analytical calculations are shown in Appendix C.

3.2 PRESSURE LOSSES

The already existing numerical model for this turbine accounts for the inducer inlet (4) until the exducer outlet (9). In this model, it is assumed that there are no pressure losses between the turbine inlet (1) and the inducer inlet (4) and between the exducer outlet (9) and the turbine outlet (12). Although these losses are extremely low they should be considered to be as much accurate as possible. These losses are calculated in this section.

The inputs needed for the existing numerical model of this turbine are the inducer inlet (section 4) total pressure and total temperature, the exducer outlet (section 9) static pressure, the rotational speed of the rotor and the inducer inlet (section 4) velocity angle which is the angle between the velocity and the volute outlet normal vector. These conditions were measured experimentally at the inlet (1) and at the outlet (12) of the turbine. For the case of the inlet velocity angle it was calculated analytically. The initial conditions for the numerical model are calculated accounting the pressure losses of the inlet and the outlet pipes of the turbine (from section 1 to 4 and from 9 to 12).

3.2.1 INLET PRESSURE LOSS

For the inlet pressure loss calculation, the initial conditions needed are the mass flow rate, the inlet (section 1) total pressure and the inlet (1) total temperature (all of them measured experimentally). Figure 3.3 shows a photo of the manufactured prototype of the turbine volute.

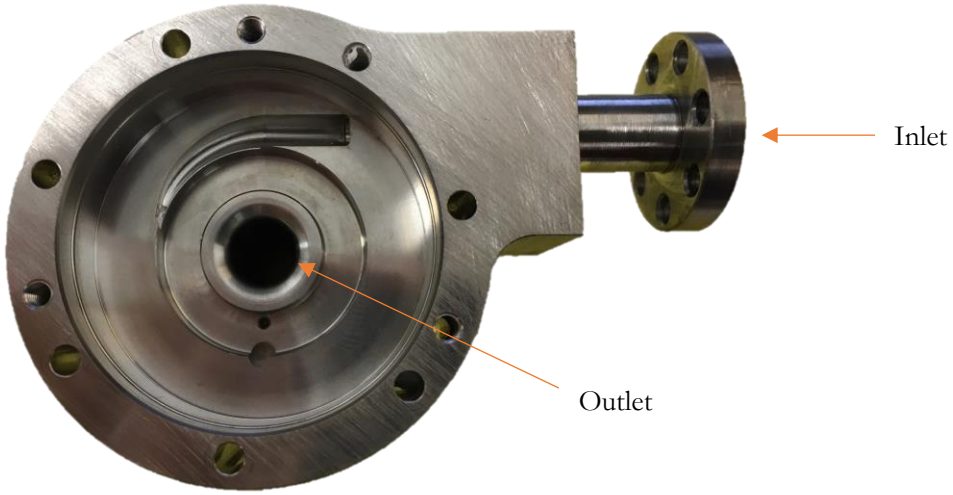

Figure 3.3 – The manufactured partial-admission turbine volute (without turbine stator)

For the analytical calculation of the turbine inlet pressure loss, the turbine inlet is divided into four sections (Figure 3.4). The first section (1-2) has a constant area and the other three sections (2 to 3, 3 to 3.1 and 3.1 to 3.2) are not constant, hence a discretization is necessary.

The highest pressure-loss is in the volute (3.1 to 3.2) due to the higher change of area and the curve of the volute.

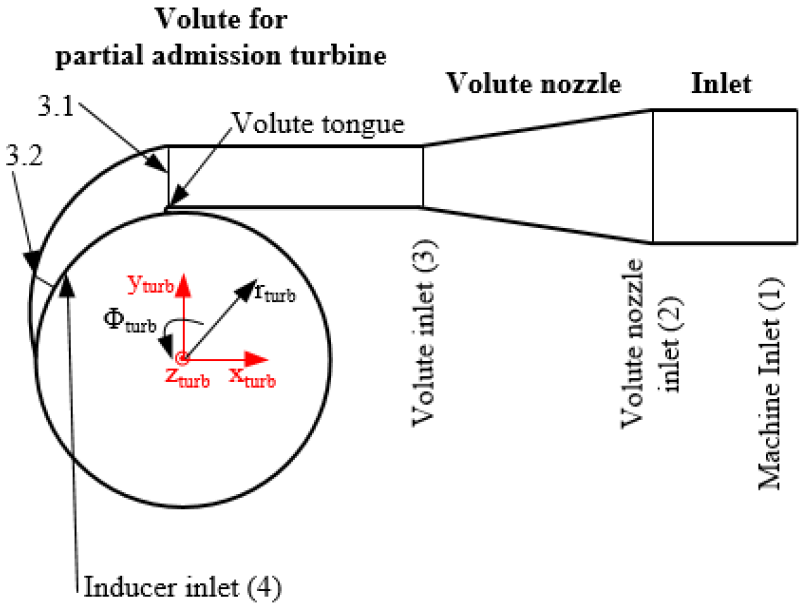

Figure 3.4 – Schematic turbine inlet with the nomenclature of the different sections. Adapted from [1].

The pressure loss of a pipe is calculated as

$$\Delta p = \frac{1}{2} \cdot f_D \cdot \rho \cdot c^2 \cdot \frac{L}{D} \tag{3.15}$$

The friction factor (f_D) used in equation (3.15) is obtained from the Moody Diagram, knowing first the Reynolds number (Re) and the relative roughness ($\frac{\varepsilon}{D}$) of the pipe. The Reynolds number is a function of the fluid density, the dynamic viscosity, the flow velocity and the diameter of each part (equation (3.16).

$$Re = \frac{\rho \cdot c \cdot D}{\mu} \tag{3.16}$$

The Moody Diagram is approximated by equation (3.17) in the straight pipes [3]

$$f_D = 0{,}0055 \cdot \left[1 + \left(2 \cdot 10^4 \cdot \frac{\varepsilon}{D} + \frac{10^6}{Re}\right)^{\frac{1}{3}}\right] \tag{3.17}$$

and by equation (3.18) in the curved pipes [4]

$$f_D = \frac{0{,}314}{0{,}95 \cdot Re^{0{,}25}} + 0{,}0075 \cdot \sqrt{\frac{D}{2 \cdot r_h}} \tag{3.18}$$

where the Reynolds number is calculated with the equation (3.16) for each of the discretized elements and r_h is the curve radius. D is the equivalent diameter of the pipe for each section and it is calculated as

$$D = R_{3.1} + b_{3.1} \tag{3.19}$$

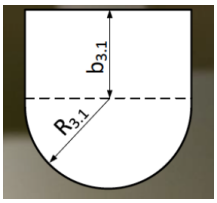

Figure 3.5 – Tunnel-type volute section shape and nomenclature

To know the relative roughness of the material ($\frac{\varepsilon}{D}$) it is necessary to know the absolute roughness (ε) to be able to divide it by the diameter. The absolute roughness has been calculated with the following simplified expression (3.20) from Adams, Grant and Watson [5] with R_a (mean roughness).

$$\varepsilon = 11{,}03 \cdot R_a \tag{3.20}$$

This mean roughness (R_a) has been measured experimentally with TESA Rugosurf 90G and it is shown and explained in appendix A. Once the absolute roughness is known, the friction factor can be calculated with the expressions shown before (3.17) (3.18).

As it was stated before, the sections with non-constant area are discretized. Figure 3.6 shows the relation between the pressure loss at the turbine inlet (from section 1 to 4) and the number of discretization elements used per part. The result converges for 1000 elements per part.

The pressure loss is also calculated for different initial conditions (mass flow rate and inlet total pressure) to verify that the model works for different situations. The different initial conditions tested are shown in Table 3.2, and the results are shown in Table 3.3.

Table 3.2 - Different initial conditions for the tested situations of the inlet analytical model

	1st situation	**2nd situation**	**3rd situation**
Mass flow [kg/h]	2,86	1,87	1,14
Inlet pressure [bar]	2,74	1,94	1,40

Table 3.3 - Results of the analytical model for the different situations

	1st situation	**2nd situation**	**3rd situation**
Pressure loss section 1-4 [mbar]	8,9	5,7	3,2

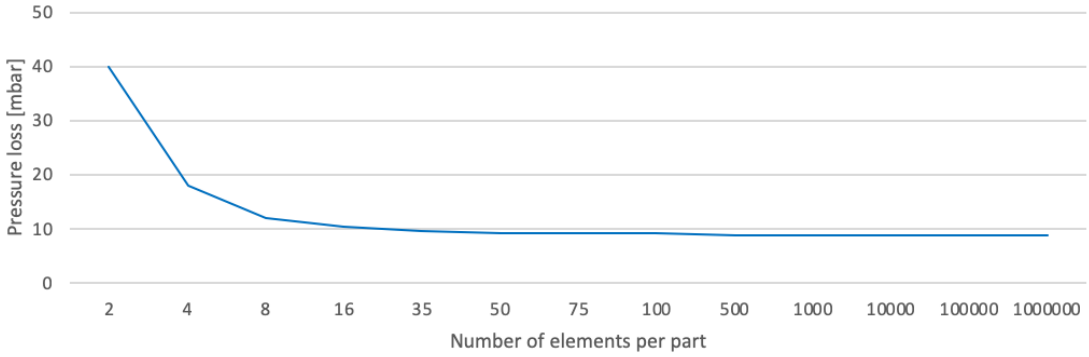

Figure 3.6 – Graphic of conversion for the inlet pressure loss for the different number of discretization elements per part

These results are used in section 5.2 to improve the inlet boundary conditions of the turbine numerical model.

3.2.2 OUTLET PRESSURE LOSS

For the outlet part of the turbine the process has been similar as for the inlet. The outlet is divided into different sections to simplify the calculations depending on the shape of each section. The expressions used for the outlet pressure loss are the same as for the inlet (3.15), (3.16), (3.17) and (3.18), the only exception is the sudden expansion loss of the transition between the exducer and the diffuser (section 9) and from the outlet of the pipe to the ambient (section 12). This sudden expansion loss in the transition part has been calculated with the following expression (3.21) [6]

$$\Delta p = \rho \cdot \frac{A_1}{A_2} \cdot \left(1 - \frac{A_1}{A_2}\right) \cdot {c_1}^2 \tag{3.21}$$

where section 1 is the area before the transition and section 2 is the area after the transition. A_1 is calculated with the factor of 33 % because it is considered that the fluid still has not expanded throughout the whole circumference. However, in section 2 the fluid is expanded to the whole tube. The expressions used to calculate these areas are

$$A_1 = \pi \cdot ({r_1}^2 - {r_2}^2) \cdot 0{,}33 \tag{3.22}$$

$$A_2 = \pi \cdot {r_1}^2 \tag{3.23}$$

For the case of the outlet to the ambient, the sudden expansion pressure loss is due to the loss of the outlet velocity, thus it is calculated with the following expression (3.24)

$$\Delta p = \frac{1}{2} \cdot \rho \cdot c^2 \tag{3.24}$$

These sudden expansion losses are added to the friction pressure losses. The complete outlet pressure loss calculated for the turbine in the nominal working point is 16,2 mbar. The outlet pressure loss is also calculated for other initial conditions to verify the model.

Table 3.4 – Different initial conditions for the tested situations of the outlet analytical model

	1st situation	**2nd situation**	**3rd situation**
Mass flow [kg/h]	2,86	1,87	1,14
Outlet pressure [bar]	0,97	0,96	0,96

Table 3.5 - Results of the analytical model for the different situations

	1st situation	**2nd situation**	**3rd situation**
Pressure loss section 1-4 [mbar]	16,2	7,0	2,6

These results are used in section 5.2 to improve the outlet boundary condition of the turbine numerical model.

3.3 VELOCITY ANGLE AT THE VOLUTE OUTLET

Another inlet boundary condition for the turbine numerical model is the fluid angle at the volute outlet (4) based on the normal vector of the volute outlet surface. Figure 3.7 shows the turbine volute with the removable turbine inducer and stator, as well as a schematic of the tunnel-type shape of the volute. The angle of the flow at the volute outlet (section 4) is caused by the curve of the turbine volute, which is a tunnel-type volute consisting of a half circle with a radius ($R_{3.1}$ in Figure 3.7) of 2 mm and a rectangular part with a height of $2 \cdot R_{3.1}$ = 4 mm at the turbine section 3.1. The volute radius decreases from 2 mm at section 3.1 to 0,56 mm at section 3.2, as defined in Figure 3.7. The volute width that is equal to the stator blade channel width ($b_{3.1}$ = 0,7 mm) is constant for the entire volute.

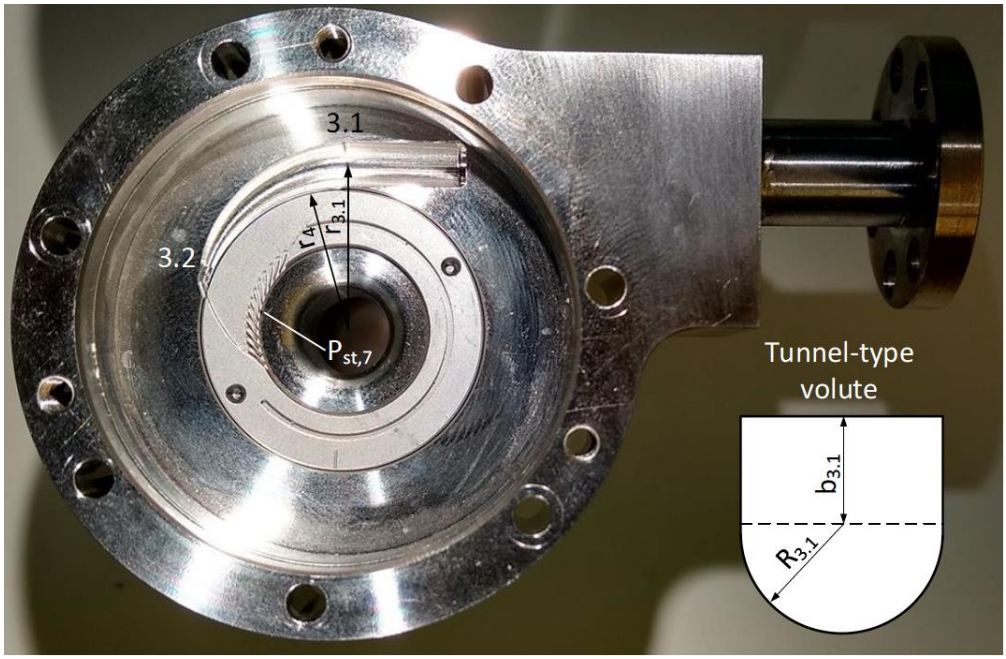

Figure 3.7 – Turbine volute with the removable turbine stator. [1]

This angle is also calculated analytically and compared to the numerical results in section 5.1.4. To calculate this angle analytically and to simplify the calculations the author uses the following assumptions: (1) the volute is perfectly designed and thus the mass flow is equally distributed along the volute outlet, and (2) the angular momentum ($r \cdot C_u = constant$) is constant, thus no friction between the fluid and the walls. Since the analytical and numerical models (see section 5.1.4) show good agreement, these assumptions are valid, even for such a small-scale turbine volute.

With these assumptions, the expression used to calculate the velocity angle between the velocity vectors and the normal vectors at the volute outlet (section 4) is

$$\alpha_4 = \tan^{-1} \frac{r_{3.1} \cdot A_4}{r_4 \cdot A_{3.1}} \tag{3.25}$$

where A_4 is the area of the volute outlet surface (section 4) and it is calculated as

$$A_4 = \epsilon_a \cdot 2 \cdot r_4 \cdot \pi \cdot b_4 \tag{3.26}$$

where $\epsilon_a = \frac{13}{61}$ is the admission ratio, r_4 is the volute outlet radius (Figure 3.7) and b_4 is the width of the volute outlet, and $A_{3.1}$ is the area of the tunnel-type volute at the volute inlet (section 3.1) and is calculated as

$$A_{3.1} = \frac{1}{2} \cdot {R_{3.1}}^2 \cdot \pi + 2 \cdot R_{3.1} \cdot b_4 \tag{3.27}$$

where $R_{3.1}$ is the radius of the tunnel-type volute section and b_4 is the width of the volute outlet.

The result for α_4 is 57,1° (see Figure 3.8). This result is compared with the numerical model result in section 5.1.4.

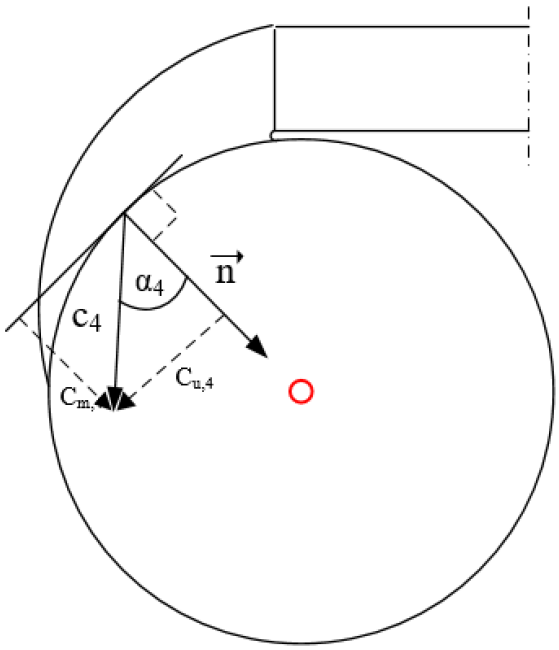

Figure 3.8 – Schematic view of the turbine volute

4 EXPERIMENTAL MEASUREMENTS

This chapter gives an overview and explains briefly the turbine experiments from Wagner [1].

4.1 TURBINE EXPERIMENT AND MEASUREMENTS

The experimental measurements and testing of the FTU unit were performed by Wagner [1]. This section gives a general overview of the Fan Turbine Unit experiments.

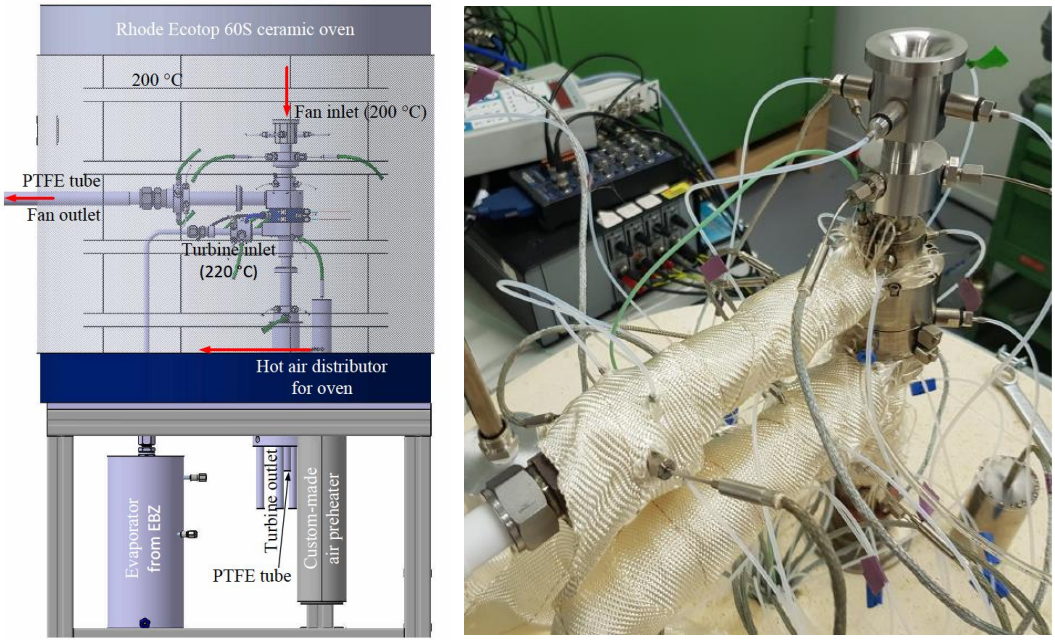

Figure 4.1 – Overview of the Fan-Turbine Unit test rig for hot air at 200 °C (fan inlet) without glass fiber insulation (left) and real implementation partly covered with glass fiber insulation without the oven cover. [1]

Figure 4.1 shows the setup of the test rig for hot air at 200 °C at the fan inlet and 220 °C for the turbine inlet. The prototype with all the measurement sensors is placed inside a ceramic oven at a constant temperature of 200 °C to simulate the real environment at the SOFC hot box. In the right photo of Figure 4.1 the real test rig is shown with some of the pipes covered with glass fiber tapes to avoid heat losses to the oven environment. The main sensors installed in the test rig are the total temperature and static pressure measurements at the inlet and at the outlet of the fan and the turbine, the mass flow rate measurement at the turbine and fan inlet and the shaft rotational speed measurement.

Chapter 5.2 states some of the results obtained from the turbine experiments with hot air at 200°C which are used to calculate the power, the isentropic efficiency and the degree of reaction. These

measurements are compared with the numerical and analytical model. The experiment was run for different rotational speeds from 100 krpm to 168 krpm (nominal speed).

Table 4.1 – Parameters measured during the turbine experiments by Wagner [1]

Situation	**1**	**2**	**3**	**4**	**5**	**6**	**7**	**8**
Rotational speed [krpm]	99,76	109,88	119,44	131,04	140,25	150,21	159,90	168,16
Mass flow rate [kg/s]	1,549	1,712	1,870	2,069	2,225	2,403	2,644	2,859
Inlet total pressure [bar]	1,693	1,816	1,938	2,096	2,216	2,364	2,557	2,735
Outlet total pressure [bar]	0,961	0,962	0,963	0,964	0,964	0,964	0,964	0,965
Inlet total temperature [ºC]	221,4	221,4	221,1	220,6	220,8	221,3	221,4	220,3
Outlet total temperature [ºC]	202,8	202,0	200,8	199,3	198,6	197,6	196,0	193,1

Table 4.1 show the parameters needed for the calculations and for the numerical simulations for 8 different situations (from 100 krpm to 168 krpm). Situation 8 is the design point (168 krpm) of this turbine for hot air at 220ºC.

5 NUMERICAL CALCULATIONS

This chapter shows and explains the numerical model for the turbine inlet and volute, as well as the numerical model for the turbine. The results are compared to the analytical results from chapter 3 and to the experimental measurements from chapter 4.

5.1 TURBINE INLET AND VOLUTE SIMULATION

5.1.1 GEOMETRY

The turbine volute geometry for this numerical model was previously built with Catia. This model is done only for the inlet part of the turbine, since the analytical method is the same for both parts. Furthermore, the outlet geometry is much simpler than the inlet as the volute (from 3.1 to 3.2 in Figure 5.1) is the most complex studied part.

The first intention was to do the simulation from the turbine inlet (section 1) to the volute outlet (section 4), since the needed boundary conditions are at the volute outlet (section 4). With this simulation the results were not feasible as the CFX solver placed a wall at the volute outlet. To solve this problem the turbine inducer was added. The final geometry used to simulate the turbine volute is shown in Figure 5.1.

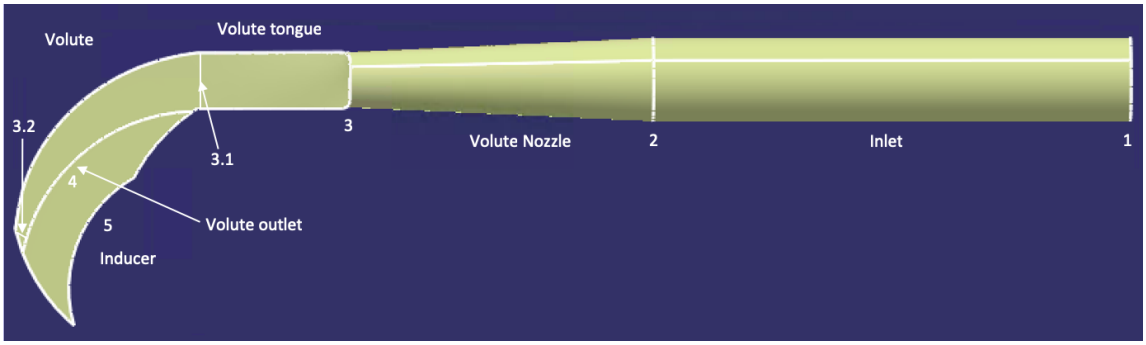

Figure 5.1 - Turbine volute and inducer geometry for the CFD simulation

5.1.2 MESH

As the geometry is split in two different parts (from section 1 to 4 and from 4 to 5), two different meshes are created. The elements of the boundary surface have to match as good as possible between both parts. After importing both geometries from Catia these meshes are created automatically with ICEM CFD. The type of elements is tetrahedral. For matching the boundary elements from both parts as good as possible the maximum size of the elements in this boundary is set. The parameter used to generate the mesh is the maximum size of the elements for each surface. In the final mesh, the maximum size of the elements is 50 μm. If the volute outlet and the inducer inlet have the same

maximum element size and the same area, they will approximately have the same number of elements and they will match correctly. To ensure that both meshes match correctly the simulation has been solved for several meshes with different number of elements.

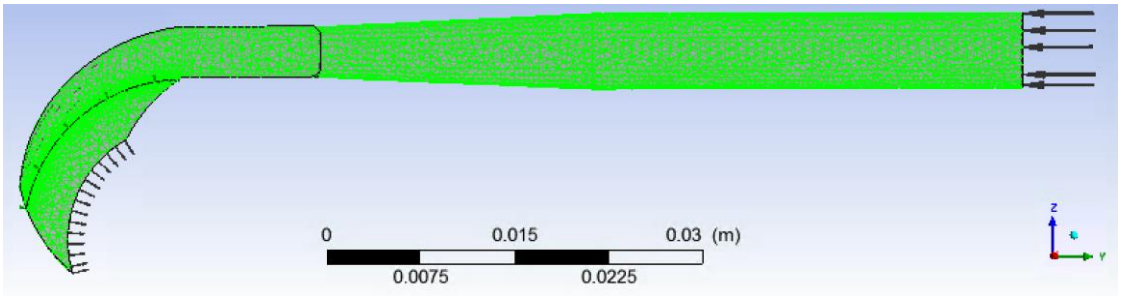

Figure 5.2 – Inlet volute and inducer domains with the generated mesh

5.1.3 RESULTS FOR THE DESIGN POINT (168 KRPM)

To verify the model and to ensure that the mesh is correct the simulation is solved for different number of mesh elements. The results are compared between the analytical model and the numerical simulation.

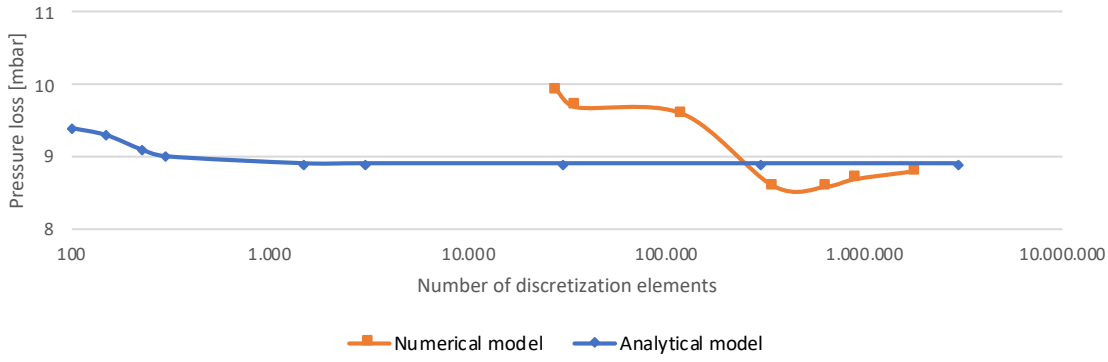

Figure 5.3 - Pressure loss graphic from the turbine inlet to the volute outlet (sections 1 to 4) of the numerical model compared to the analytical results (at 168 krpm)

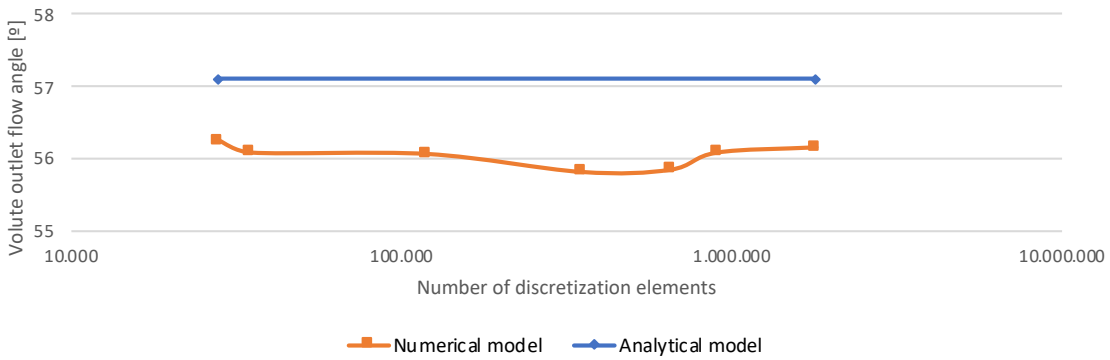

Figure 5.4 - Velocity angle at the volute outlet (section 4) graphic of the numerical model compared to the analytical result (at 168 krpm)

Figure 5.3 and Figure 5.4 show respectively, the results of the pressure loss and the volute outlet velocity angle for different number of mesh elements. The simulation is solved for 28k, 35k, 125k, 350k, 900k and 1,8m mesh elements. The number of elements that optimized the accuracy of the results with a reasonable solving time is the one with 900k elements. The results of the simulation are 8,7 mbar (900k mesh elements) for the inlet pressure loss and 56,1º for the volute outlet velocity angle for the design situation (168 krpm).

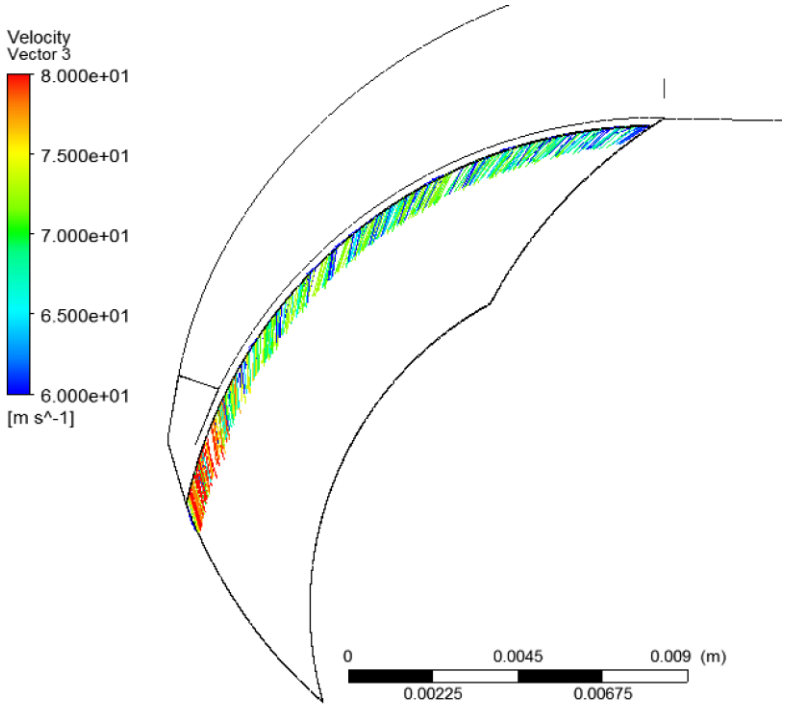

Figure 5.5 – Velocity vectors at the volute outlet

Figure 5.5 shows how the velocity vectors at the volute outlet are distributed equally. This would mean that the turbine volute has been designed correctly.

5.1.4 COMPARISON BETWEEN NUMERICAL AND ANALYTICAL RESULTS FOR THE DESIGN POINT (168 KRPM)

After calculating the inlet pressure loss and the velocity angle with the analytical and the numerical models, they are compared to see the difference between them and to verify the models.

Table 5.1 - Analytical and numerical results comparison for the design point (168 krpm)

	Analytical	**Numerical**	**Difference**
Inlet pressure loss [mbar]	8,9	8,8	1,1 %
Volute outlet velocity angle [º]	57,1	56,2	1,6 %

As shown in Table 5.1 the results of both models are very similar, with an error of 1,1 % for the inlet pressure loss and 1,6 % for the velocity angle at the volute outlet (both based on the analytical value). The difference between the analytical and the numerical results are due to the assumptions made at the analytical calculation. These assumptions are explained in section 3.3. As in the numerical model the friction between the fluid and the walls of the pipe is considered, the angle is expected to be lower,

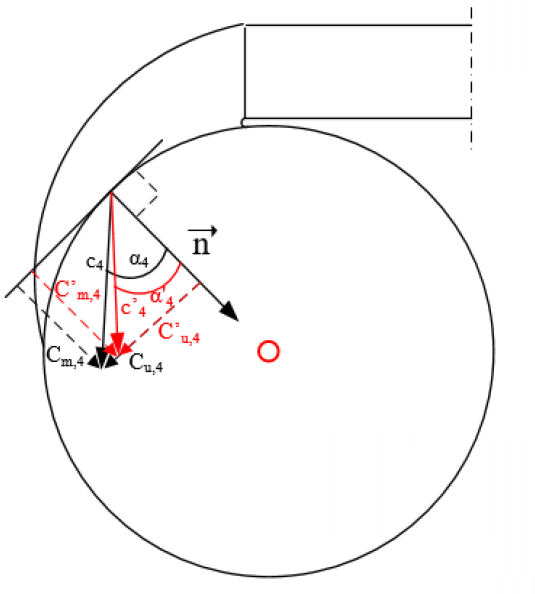

Figure 5.6 – Schematic view of the turbine outlet with the velocity vectors calculated analytically (black) and numerically (red)

since $r \cdot C_u$ is not constant (see Figure 5.6). As the deviation between both models is very low, both numerical and analytical models are considered to be verified. Results are shown schematically in Figure 5.6, the analytical results are shown in black and the numerical results in red.

The results used for the definition of the inlet boundary conditions of the numerical turbine model of the following sections will be the numerical ones, since these are considered as more accurate. The analytical model will be used to define the outlet boundary condition of the turbine.

5.2 TURBINE SINGLE PASSAGE SIMULATION

The results of the inlet pressure loss, the outlet pressure loss, and the velocity angle at the volute outlet are used to solve the complete CFD simulation for the turbine domain. The boundary conditions at the inlet and at the outlet are adapted with the results of the previous chapters. The simulation only models one single passage including one stator blade and one rotor blade. This is explained in detail in section 5.2.1.

5.2.1 STATIONARY SIMULATION

The simulation domain (see Figure 5.7) consists of the turbine inducer, the turbine stator, the turbine rotor and the turbine exducer. The stator has 12 blades and features an admission of $\frac{12+1}{61} = 0{,}21$. Although the real turbine rotor has 59 blades, in the CFD simulation it has 61 blades to realize a frozen rotor interface between the stator and the rotor with no pitch change. The rotor pitch in the simulation is therefore 3,3% smaller than the pitch of the real turbine rotor.

The inlet boundary conditions (section 4) are the total pressure, the total temperature and the absolute flow angle. The turbine inlet from the turbine section 1 to 4 is assumed adiabatic and thus the total temperature is constant from section 1 to 4, this total temperature was measured experimentally. The pressure loss between 1 and 4 (Δp_{1-4}) is calculated in section 5.1 and is 8,7 mbar (8,9 mbar analytically) for the nominal working point. So, the CFD inlet total pressure ($p_{t,inlet,CFD}$) is the total pressure measured experimentally at section 1 ($p_{t,inlet}$) minus the pressure loss calculated (equation (5.1).

$$p_{t,inlet,CFD} = p_{t,4} = p_{t,inlet} - \Delta p_{1-4} \tag{5.1}$$

The absolute flow angle at the inlet is calculated in section 3.3 analytically and in section 5.1 numerically. The result used for the turbine simulation is the numerical one and is 56,1° (angle between the absolute flow and the normal vector of the volute outlet surface).

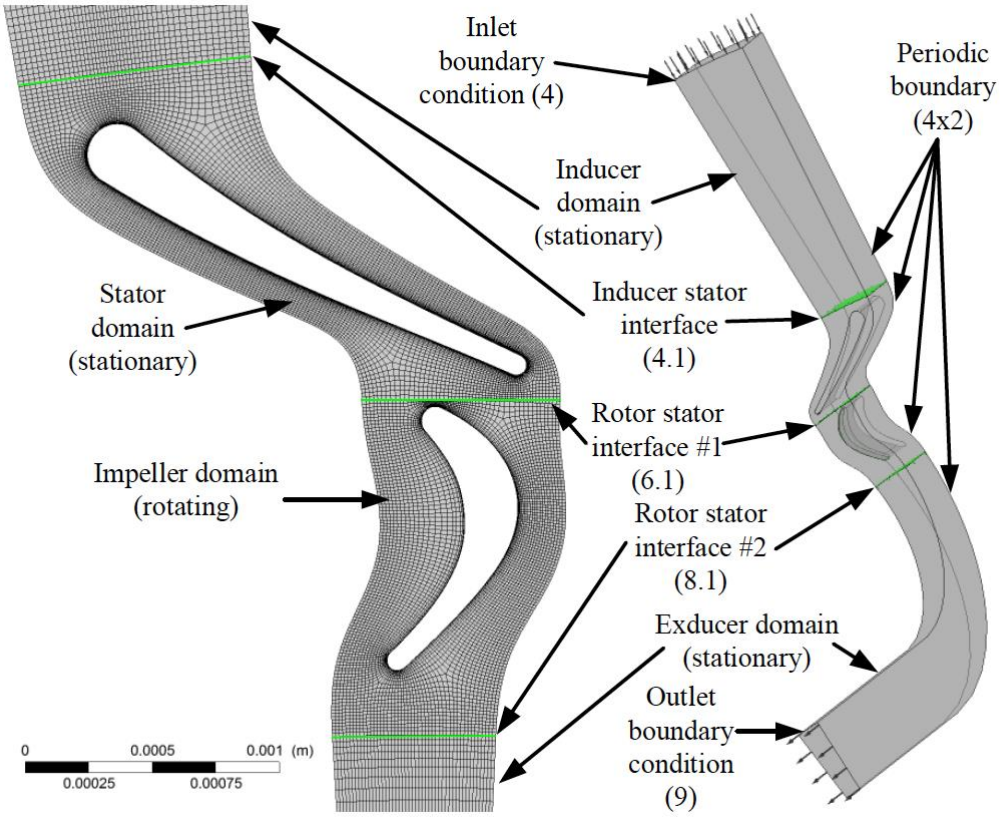

Figure 5.7 – Domain regions (right): inducer, stator, rotor and exducer domain from the top to the bottom and generated mesh (left) at the hub for each domain from the bottom view. Fluid-to-fluid interfaces are marked in green. [1]

The outlet boundary condition (turbine section 9) is the static pressure ($p_{s,9}$), hence the mass flow rate through the passage is the result of the simulation. As for the inlet section, the outlet boundary condition takes the pressure loss that is calculated in section 3.2 into account (sudden expansion loss and frictional loss). This outlet pressure loss (Δp_{9-12}) is 16,2 mbar for the nominal point. So, the static outlet pressure is the outlet pressure measured experimentally (ambient pressure) plus the pressure loss from 9 to 12 calculated in the previous chapters minus the dynamic pressure (pressure caused by the velocity at section 9). For the dynamic pressure the velocity is calculated in the first place with the mass flow rate and the area at section 9.

$$p_{s,outlet,CFD} = p_{s,9} = p_{t,outlet} + \Delta p_{9-12} - \frac{1}{2} \cdot \rho \cdot {c_9}^2 \tag{5.2}$$

The stationary exducer domain hub assumes a rotating wall with the rotational speed of the rotor domain. The rotational speed at the nominal working point is 168,2 krpm.

Table 5.2 - CFD boundary conditions used for the nominal working point

	Value	Units
Rotational speed	168,2	[krpm]
Inlet total pressure (4)	2,726	[bar]
Inlet total temperature (4)	220,3	[ºC]
Inlet absolute flow angle (4)	56,1	[º]
Outlet static pressure (9)	0,926	[bar]

The measured mass flow in the experiment is 2,86 kg/h and the result of this CFD simulation is 13·0,264 = 3.43 kg/h which is equal to a difference of 0,57 kg/h. This could be caused by three different reasons:

1- The distance between the stator blades is lower due to the manufacturing limitation. This leads to a measured minimum distance between stator blades between 0,18 and 0,23 (see Figure 5.8), whereas it is 0,23 in the CFD simulation. Thus, there is an error between 0-22% because of the difference of passing area.
2- The difference in the geometry between the CFD inducer and the reality. In reality the inducer side walls have a displacement of the boundary layer of around 0,04 mm. This results in a partial blocking of the first and the last stator blade rows and thus in an overall blockage of all the stator blade rows. The CFD single passage simulation does not account for these two side walls effects.
3- The manufactured stator blades have a roughness based on the arithmetical mean deviation (Ra) of about 0,002 mm resulting in a 1,2% lower critical area.

These three facts could be the reason of the higher mass flow rate for the simulation and thus a higher power.

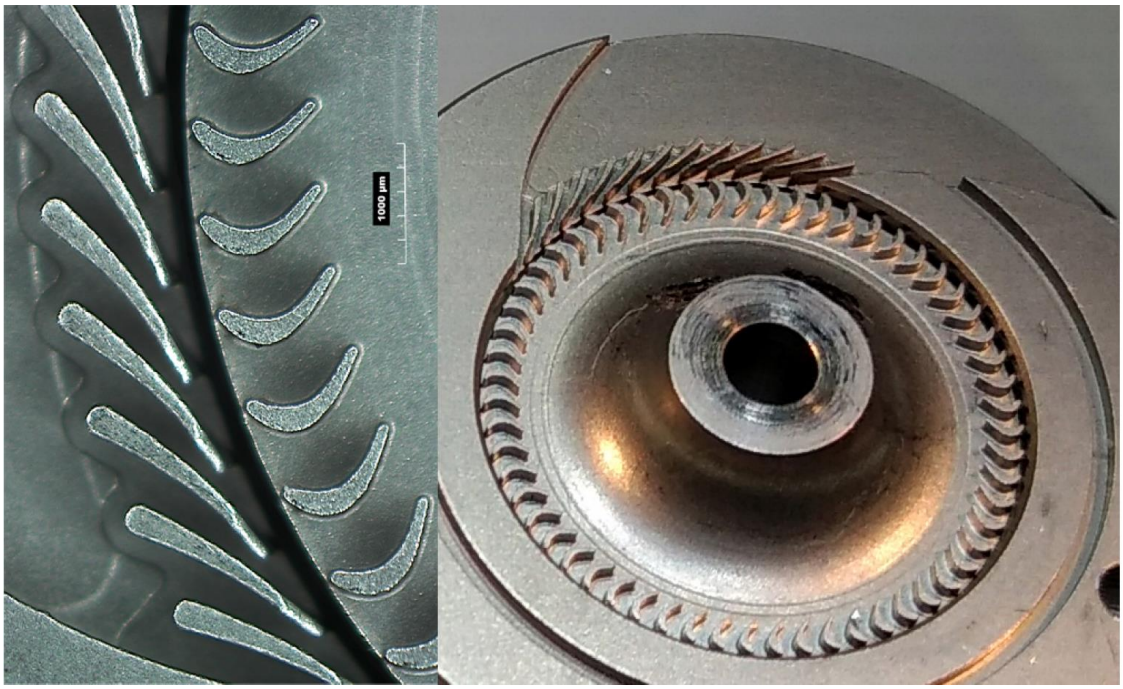

Figure 5.8 – Optical microscopy with Hirox KH-8700 (left) of the turbine stator and rotor (digitally mirrored) and overview of turbine stator and rotor (upside-down) with turbine inducer (right). [1]

In order to compare the CFD simulation and the experiment, the power is corrected with the mass flow relation between the simulation and the experiment.

$$P_{CFD,corrected} = \frac{P_{CFD}}{\dot{m}_{CFD}} \cdot \dot{m}_{exp} \tag{5.3}$$

In the previous case (for the nominal conditions) the power in the CFD for single passage is 3,71 W and the mass flow in the CFD single passage simulation is 0,26 kg/h. With the experimental mass flow of 2,86 kg/h, the corrected power result from the CFD is 40,2 W. The power that was measured experimentally by Wagner [1] is 21,9 W. If the gas film mechanical loss (18 W) is added to the measured power, the turbine power is 39,9 W.

The degree of reaction is another measurement used to compare the results of the experimental measurements with the numerical simulations. The degree of reaction is defined in first approximation

as the ratio of static pressure drop in the rotor to the static pressure drop in the stage, since the static enthalpy difference in the rotor and the static enthalpy difference in the stage are not measured.

$$\delta_h = \frac{\Delta p_{s,rotor}}{\Delta p_{t,rotor+stator}} \tag{5.4}$$

In the experiments performed by Wagner [1] the degree of reaction for the nominal working point is 0,15. For this calculation, Wagner [1] measured experimentally the static pressure between the rotor and the stator in a specific hole made between them. At the CFD simulation, the degree of reaction for the same boundary conditions was 0,22, a 47% higher. This difference is caused by the difference of the total pressure at the outlet ($p_{t,9}$) between the CFD simulation and the real experiment, and this difference of total pressure is mainly caused by the difference of velocity. This velocity is higher in the CFD because the area where the fluid goes through is constant through all the single passage (21% of the circumference) and in reality, it expands to a higher proportion of the circumference. To correct this error the outlet static pressure ($p_{s,9}$) is adjusted with the outlet total pressure ($p_{t,9}$), and the velocity (Mach number) of the previous CFD simulation (equation (5.5).

$$p_{s,9} = p_{t,9} \cdot (1 + \frac{k-1}{2} \cdot Ma^2)^{\frac{-k}{k-1}} \tag{5.5}$$

where $p_{t,9}$ is the total pressure at the outlet which is calculated adding the outlet pressure loss from section 3.2.2 to the ambient pressure measured experimentally, and Ma is the Mach Number which is calculated at the previous iteration by the CFD simulation.

This iterative process is done two times to see the behavior of the degree of reaction, the power of the turbine and the efficiency. Table 5.4 shows the results of the two iterations for the reaction, the turbine power and the efficiency at the design point (168 krpm).

Table 5.3 – Total pressure calculated for the outlet boundary condition and total pressure at the outlet of the CFD simulation for each iteration at the design point (168 krpm)

	$p_{t,calculated}$	$p_{t,simulation}$
CFD simulation	0,98	1,18
CFD iteration 1 (corrected $p_{s,9}$)	0,98	1,09
CFD iteration 2 (corrected $p_{s,9}$)	0,98	1,05

Table 5.4 - Experimental measurements and CFD simulation results for the different iterations for the degree of reaction and power (corrected $p_{s,9}$) at the design point (168 krpm)

	Reaction	**Power [W]**	**Efficiency**
Experimental measurement	0,15	39,9	0,39
CFD simulation	0,22	40,2	0,38
CFD iteration 1 (corrected $p_{s,9}$)	0,18	42,7	0,35
CFD iteration 2 (corrected $p_{s,9}$)	0,16	43,4	0,45

As it can be observed in Table 5.4, while the degree of reaction decreases to move closer to the experimental measurement, the power of the turbine increases and the efficiency decreases and both move further from the experimental measurement. This is caused by the change of the outlet total pressure.

The single-passage simulation is also solved for other boundary conditions that were measured previously by Wagner [1] and the same iterative procedure has been carried out for some of them. Results are shown in the following figures.

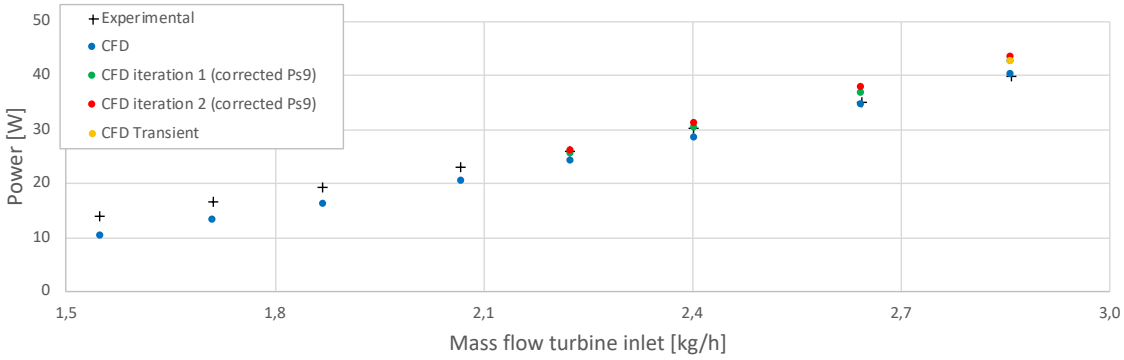

Figure 5.9 - Turbine power graphic comparison between the experiments and the CFD simulations

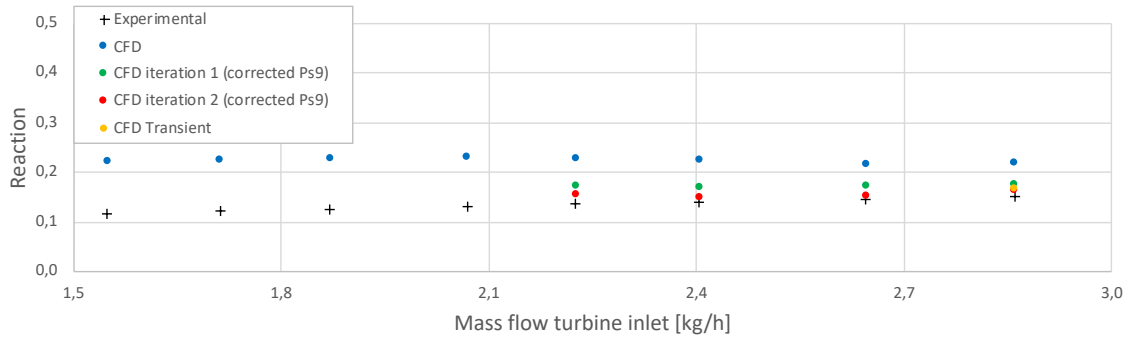

Figure 5.10 – Degree of reaction graphic comparison between the experiments and the CFD simulations

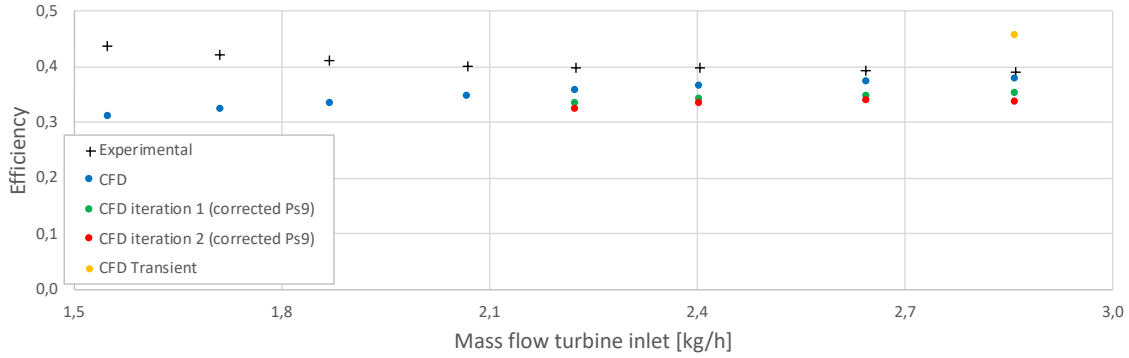

Figure 5.11 – Isentropic efficiency graphic comparison between the experiments and the CFD simulations

Figure 5.9 shows the turbine power for the different boundary conditions. As it can be observed, the turbine power is more similar between the CFD and the experiments as closer to the design point (168 krpm and 2,86 kg/h). The same behavior can be observed in Figure 5.10 with the degree of reaction and in Figure 5.11 with the isentropic efficiency. These three figures show the results shown in Table 5.4 for the rest of the measured points.

There is also a deviation between the CFD simulation and the experimental degree of reaction which is caused by the difference in measuring between both models. In the experiment, the rotor stator static pressure is measured when the rotor is running at 168 krpm at one specific hole between the rotor and the stator.

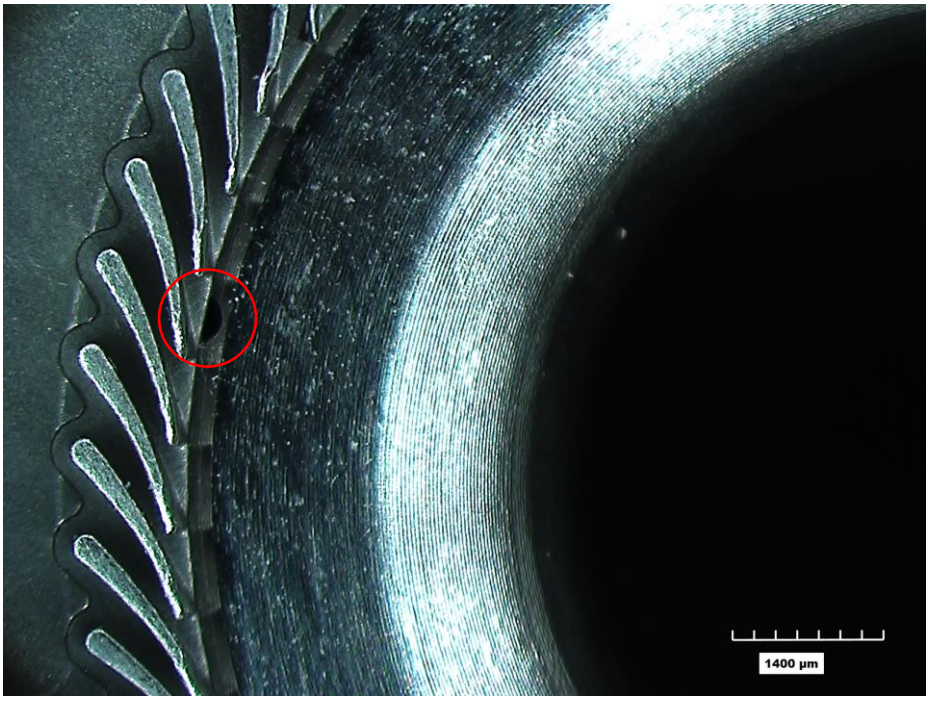

Figure 5.12 – Hole made between the rotor and the stator to measure the static pressure experimentally

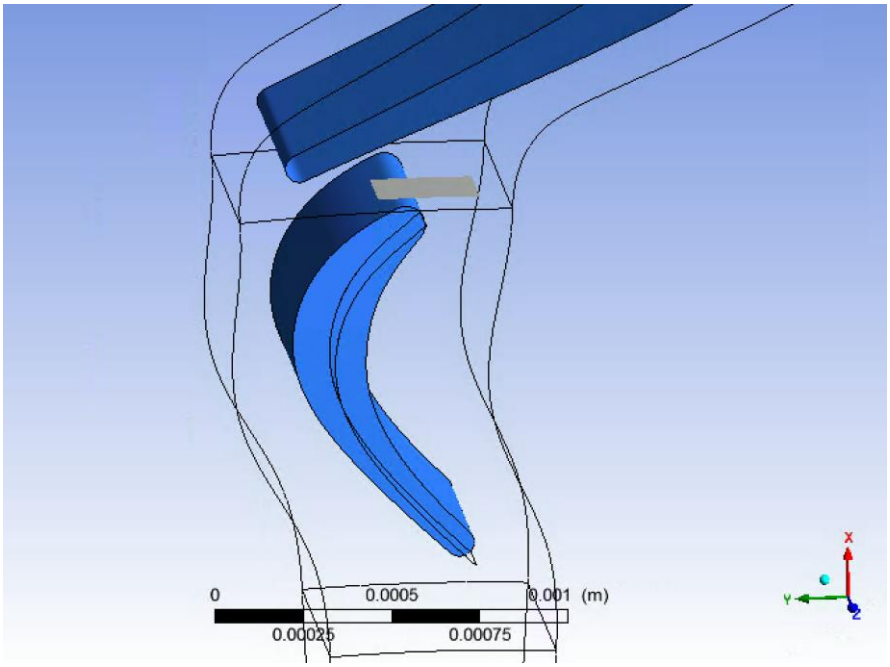

Figure 5.13 - Rotor-stator surface, simulating the real hole of the turbine, to calculate the static pressure at the CFD simulation (the span of the surface is higher for visualization, normally it is placed only at the shroud surface, span 0,99 to 1)

The pressure in this hole (see Figure 5.12) is changing continuously and extremely fast due to the rotating turbine impeller blades, thus the measured static pressure is the average of all the different static pressures at that point. However, the performed CFD simulation is steady and thus the turbine blades are not moving. To calculate the rotor stator static pressure in the CFD simulation, a surface is created (Figure 5.13) simulating the hole of the real turbine. This surface is placed approximately as it is in reality, it occupies a 40 % of the one passage rotor stator surface. The results for this surface are different to the experimental measurements, thus the author decided to try the measurement calculating this pressure all around the circumference. The CFD rotor stator static pressure is also measured for a surface placed all around the rotor (Figure 5.14), and the results are much closer to the experimental measurements. Hence, the rotor stator static pressure should be measured with the surface shown in Figure 5.14.

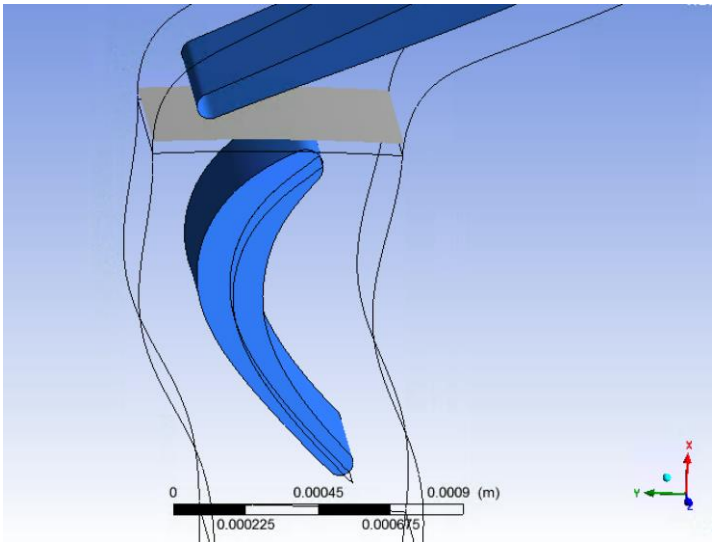

Figure 5.14 - Rotor-stator surface to calculate the static pressure at the CFD simulation with a higher span for visualization (for the calculation it is placed at the shroud surface, span 0,99 to 1)

5.2.2 TRANSIENT SIMULATION

In this section, a transient single-passage simulation is run to compare the results with the stationary simulation and analyze the differences. The transient simulation is only solved for the nominal working point with the corrected outlet pressure ($p_{s,9}$) from the second iteration. It is also initialized with the results' file of this second iteration for the nominal conditions.

The passing period (passing time for one blade) defined for this simulation is $5{,}9 \cdot 10^{-6} s$. The number of timesteps per period defined is 100, thus every timestep is $5{,}9 \cdot 10^{-8} s$. The simulation is run for 2

periods, thus the total number of timesteps is 200. The volume averaged Courant number of this simulation is 1,8 for the rotor domain and 1,1 for the stator domain. It could not be run with a lower Courant number due to the lack of time.

$$C = \frac{c \cdot \Delta t}{\Delta x} \tag{5.6}$$

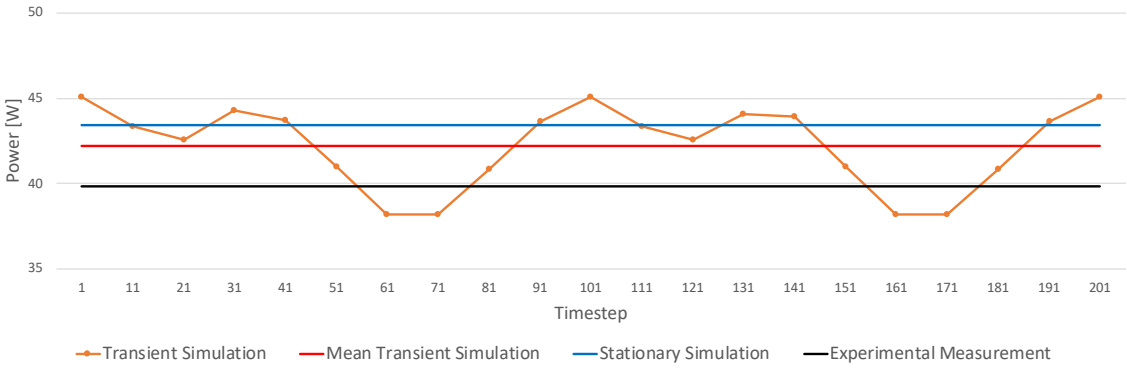

Figure 5.15 - Specific power graphic comparison between the experimental measurement, the stationary simulation and the transient simulation

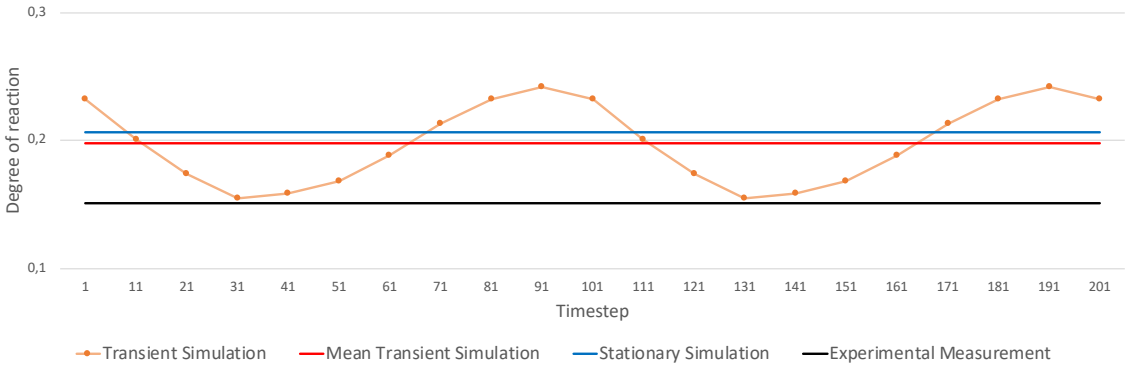

Figure 5.16 - Degree of reaction graphic comparison between the experimental measurement, the stationary simulation and the transient simulation (rotor-stator static pressure measured with the surface shown in Figure 5.13 with span 0.99 to 1)

As explained previously, the degree of reaction is calculated with the rotor stator static pressure (equation (5.4), and this pressure is evaluated experimentally and numerically. For the transient

numerical simulation, a surface is placed between the rotor and the stator as shown in Figure 5.13 and in Figure 5.14. As explained before, the static pressure calculated with the surface in Figure 5.14 is closer and more similar to the experimental measurements, even in the transient simulation.

Considering all the rotor-stator surface as in Figure 5.14, the results are much closer to the experiments, hence this surface is a better approximation to calculate the rotor-stator static pressure.

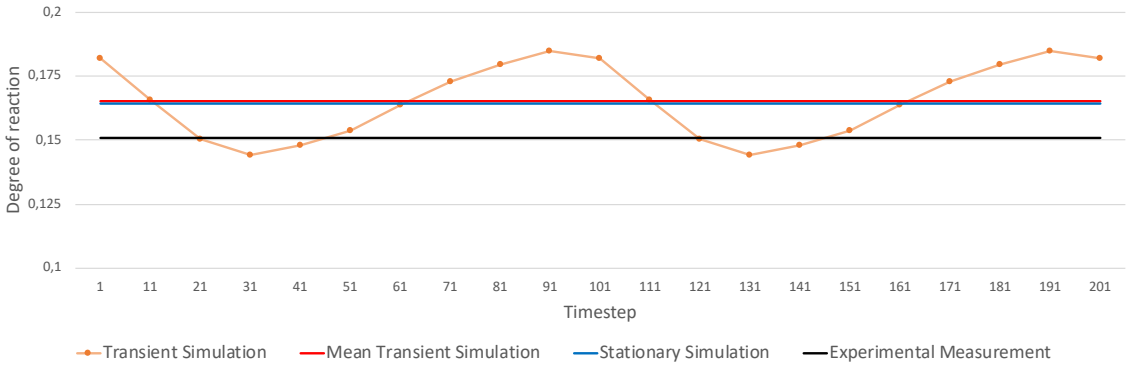

Figure 5.17 - Degree of reaction graphic comparison between the experimental measurement, the stationary simulation and the transient simulation (rotor-stator static pressure measured as in Figure 5.14)

The transient simulation results are similar to the stationary results after the two iterations of the outlet static pressure. The transient simulation is a bit closer to the experimental measurements. However, considering the difference of solving time between the stationary (1-hour wall clock for a workstation with 12 processors) and the transient simulation (12 hours, just for 2 blade periods), the stationary simulation can also be used as an approximate model for this turbine, correcting the outlet static pressure with the outlet velocity.

The transient simulation results of the power, the degree of reaction and the isentropic efficiency are also shown in Figure 5.9, Figure 5.10 and Figure 5.11 where are compared with the experiments and the stationary simulation for the three iterations at the design point.

6 CONCLUSION

6.1 SUMMARY

This thesis presents the results of the analytical and the numerical investigation of a small-scale radial-inflow turbine. This turbine propels a micro-fan to recirculate the non-burned hydrogen and the water vapor of a Solid Oxide Fuel Cell system. The main objective of the project is to improve an existing numerical model for the turbine.

In the first part of this thesis the boundary conditions for this model are adapted calculating the inlet and outlet pressure losses and the flow angle at the simulation domain inlet. These calculations are verified by an analytical and a numerical model. For the nominal conditions, the results are 8,7 mbar for the inlet pressure loss, 16,2 mbar for the outlet pressure loss and 56,1° for the flow angle at the simulation domain inlet.

The second part of this thesis suggests improvements for the existing numerical model of the turbine after adding the adapted boundary conditions of the first part. A suggested improvement is to correct the static pressure at the outlet with the outlet velocity. This error is due to the fact that the simulation is a single-passage simulation and the flow passing-area is much lower than if the fluid could expand. This error could also be caused by the fact that the simulation is stationary. A transient simulation is run at the end of this thesis to compare the results.

After comparing results from the analytical calculations, the experiments and the different simulations, the final conclusion is that the best model (accuracy vs solving time) is the stationary single passage with the corrected outlet static pressure.

The final results for the power are 38 W for the analytical model, 43 W for the stationary single-passage simulation (corrected outlet static pressure), 42 W for the transient single-passage simulation (corrected outlet static pressure) and 40 W for the experimental measurements if the bearing heat losses are added. The degree of reaction is also compared and the final results are 0,15 for the experimental measurements, 0,16 for the stationary single-passage simulation (corrected outlet static pressure) and 0,16 for the transient single passage simulation (corrected outlet static pressure).

A. MEAN ROUGHNESS EXPERIMENTAL MEASUREMENT (RA)

The roughness of the inlet pipe's surface is necessary to calculate the inlet pressure loss analytically (Chapter 3.2). This roughness is measured with the TESA Rugosurf 90G. This tool is used to measure the rugosity of plane and curved surfaces. In this case, it was used to measure the inlet pipe roughness as it is shown in Figure A.1. Since the outlet pipe was manufactured with the same material and the same machine as the inlet pipe, the outlet roughness is assumed similar.

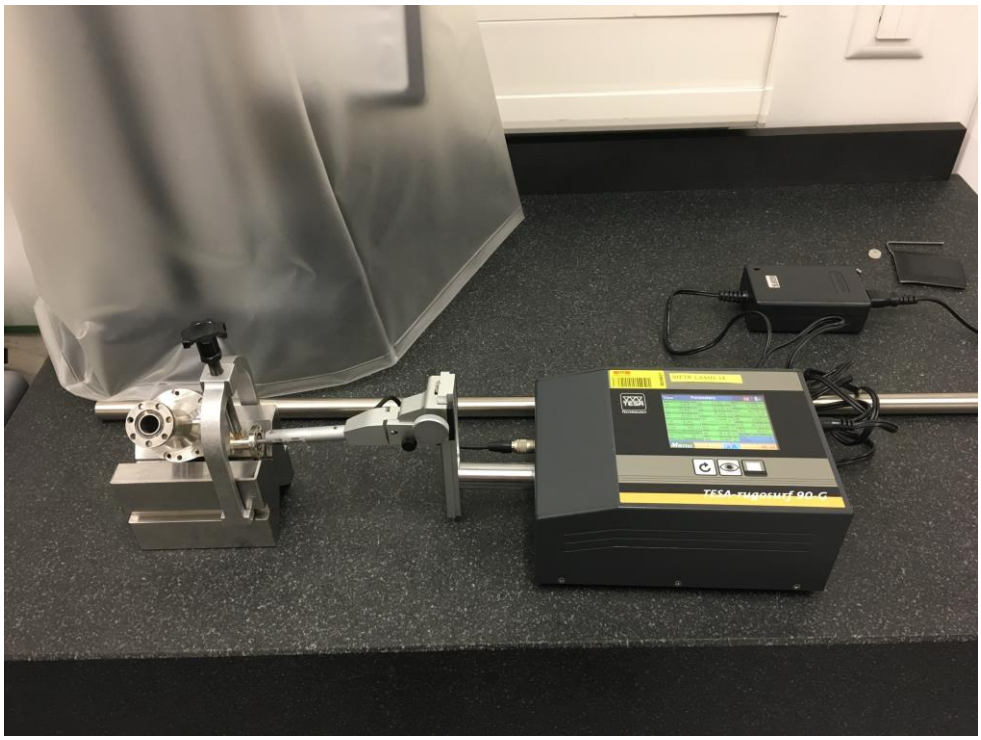

Figure A.1 - Experimental measurement of the inlet pipe surface roughness with TESA Rugosurf 90G

This tool measures the mean roughness of the surface (R_a) that is necessary for the analytical calculation (see equation (3.20). To avoid an experimental error of the measurement, it was performed several times. The roughness used for the pressure loss calculation is the average of these measurements: 3.2 μm.

Figure A.2 – TESA Rugosurf 90G's display after one of the measurements

As it is explained in section 3.2.1 the friction coefficient f_D (see equations (3.17 and (3.18) is calculated with a simplified expression of the Moody Diagram. These expressions calculate the friction coefficient from the Reynolds number (Re) and the relative roughness of the material ($\frac{\varepsilon}{D}$). To calculate the absolute roughness (ε) from the mean roughness (Ra) it has been used the simplified expression from explained in chapter 3.2 from Adams, Grant and Watson [5].

B. OTHER RESULTS CFD SIMULATIONS

As shown in section 5.2.1, the stationary single-passage CFD simulation was run for the different situations measured in the experiments. This section shows the boundary conditions and the results for all these different situations.

	Situation	1	2	3	4	5	6	7	8
Boundary conditions	Rotational speed [krpm]	99,76	109,88	119,44	131,04	140,25	150,21	159,90	168,16
	Inlet total temperature (1) [°C]	221,4	221,4	221,1	220,6	220,8	221,3	221,4	220,3
	Measured inlet total pressure (1) [bar]	1,693	1,816	1,938	2,096	2,216	2,364	2,557	2,735
	Inlet pressure loss numerical model (1-4) [bar]	0,0050	0,0055	0,0059	0,0065	0,0069	0,0074	0,0080	0,0087
	Inlet pressure loss analytical model (1-4) [bar]	0,0047	0,0052	0,0058	0,0064	0,0069	0,0075	0,0082	0,0088
	Corrected inlet (4) total pressure [bar]	1,688	1,810	1,932	2,089	2,209	2,357	2,549	2,726
	Volute outlet velocity angle numerical model (4) [°]	56,1	56,1	56,1	56,1	56,1	56,1	56,1	56,1
	Volute outlet velocity angle analytical model (4) [°]	57,1	57,1	57,1	57,1	57,1	57,1	57,1	57,1
	Measured outlet total pressure (12) [bar]	0,961	0,962	0,963	0,964	0,964	0,964	0,964	0,965
	Outlet pressure loss analytical model (9-12) [bar]	0,0048	0,0058	0,007	0,0085	0,0098	0,0115	0,0139	0,0162
	Outlet total pressure (9) [bar]	0,966	0,968	0,970	0,972	0,974	0,976	0,978	0,981

Figure B.1 – Boundary conditions for the different simulations

	Situation	1	2	3	4	5	6	7	8
Static pressure [bar]	Corrected outlet static pressure (it. 0) [bar] ($Ps_{9,0}$)	0,950	0,948	0,946	0,943	0,941	0,937	0,931	0,926
	Corrected outlet static pressure (it. 1) [bar] ($Ps_{9,1}$)					0,824	0,810	0,794	0,775
	Corrected outlet static pressure (it. 2) [bar] ($Ps_{9,2}$)					0,780	0,764	0,735	0,703
Total pressure [bar]	CFD iteration 0 ($Ps_{9,0}$)	1,0508	1,0678	1,084	1,1031	1,115	1,1306	1,150	1,1793
	CFD iteration 1 ($Ps_{9,1}$)					1,0311	1,0387	1,0629	1,0885
	CFD iteration 2 ($Ps_{9,2}$)					1,0017	1,0055	1,0291	1,0543
	CFD Transient ($Ps_{9,2}$)								1,0543

Figure B.2 – Static and total pressures for the different iterations

	Situation	1	2	3	4	5	6	7	8
Power [W]	Experimental measurement	14,04	16,62	19,30	22,87	26,01	30,08	35,04	39,86
	CFD iteration 0 ($Ps_{9,0}$)	10,28	13,15	16,20	20,46	24,11	28,55	34,58	40,18
	CFD iteration 1 ($Ps_{9,1}$)					25,62	30,36	36,67	42,69
	CFD iteration 2 ($Ps_{9,2}$)					26,14	31,07	37,68	43,40
	CFD Transient ($Ps_{9,2}$)								42,38
Degree of reaction	Experimental measurement	0,116	0,121	0,125	0,131	0,136	0,139	0,146	0,151
	CFD iteration 0 ($Ps_{9,0}$)	0,223	0,225	0,228	0,230	0,227	0,225	0,217	0,221
	CFD iteration 1 ($Ps_{9,1}$)					0,173	0,170	0,173	0,176
	CFD iteration 2 ($Ps_{9,2}$)					0,156	0,149	0,152	0,165
	CFD Transient ($Ps_{9,2}$)								0,165
Efficiency	Experimental measurement	0,438	0,423	0,412	0,402	0,400	0,400	0,393	0,392
	CFD iteration 0 ($Ps_{9,0}$)	0,313	0,325	0,335	0,349	0,360	0,368	0,376	0,381
	CFD iteration 1 ($Ps_{9,1}$)					0,336	0,344	0,350	0,354
	CFD iteration 2 ($Ps_{9,2}$)					0,327	0,336	0,340	0,338
	CFD Transient ($Ps_{9,2}$)								0,458

Figure B.3 – Power, degree of reaction and efficiency results for the different simulations

Figure B.3 show the results of the power, the degree of reaction and the efficiency of all the CFD simulations run in this thesis. The CFD simulation with an assumed outlet velocity was run for the 8 different boundary conditions shown in Figure B.1. However, the iterative process to correct the outlet total pressure was only run for the last 4 situations, whereas the transient simulation just for the 8th simulation (design point: 168 krpm). Figure B.2 show the different static pressures (outlet boundary condition) for these simulations and the result of the total pressure at section 9, to see the difference with the calculated total pressure (in Figure B.1).

C. MATLAB SCRIPTS

C.1. VOLUTE INLET PRESSURE LOSS

```
%to calculate the pressure loss from the inlet of the turbine to the
%inducer inlet (1-4)
%inputs: T_inlet, P_inlet, m_dot, Ra (Roughness)

m_dot=2.859; %input
T_inlet=220.31; %input
P_inlet=2.7347; %input
Ra=3.172; %input
epsilon=Ra*10^-3*11.03; %absolute roughness
P_atm=0.9643; %atmospheric pressure
Prel_inlet=P_inlet-P_atm; %inlet relative pressure

%calculations
R=286.9; %gas constant
density=P_inlet*10^5/(R*(T_inlet+273.15)); %(kg/m^3)

%section 1 to 2
r12=3; %(mm)
A12=pi*r12^2; %(mm^2)
c12=m_dot /(density*3600*A12*10^-6); %(m/s)
D12=2*r12; %(mm)
L12=34.25; %(mm)

%moody
Re12 = density*c12*D12*10^-3/(1.74*10^-5); %Reynolds number
lambda12 = 0.0055*(1+(2*10^4*(epsilon/D12)+10^6/Re12)^(1/3)); %friction
%coefficient from aproximation of the moody diagram

AP12=lambda12*0.5*density*c12^2*L12*10^-5/D12; %pressure loss section 1-
2
APtotal_1=AP12; %total pressure loss
Prel_2=Prel_inlet-AP12; %relative pressure at point 2

%section 2 to 3
%discretize in j sections
APtotal_2=APtotal_1;
AP23=0;
j=1000000;
for i=1:j
    r2i=r12-(i/j)*1;
    A2i=pi*r2i^2;
    c2i=m_dot/(density*3600*A2i*10^-6);
    D2i=r2i*2;
    L2i=21.866/j;
    Re2i = density*c2i*D2i*10^-3/(1.74*10^-5);
    lambda2i = 0.0055*(1+(2*10^4*(epsilon/D2i)+10^6/Re2i)^(1/3));
    AP2i=lambda2i*0.5*density*c2i^2*L2i*10^-5/D2i;
    AP23=AP23+AP2i;
    APtotal_2=APtotal_2+AP2i;
end
```

```
Prel_3=Prel_2-AP23;

%section 3 to 3.1
%discretize in u sections
APtotal_3=APtotal_2;
AP34=0;
u=1000000;
for n=1:u
    r3n=2;
    A3n=((pi*r3n^2/2)+(2.2-((2.2-0.7)*(n/u)))*2*r3n);
    c3n=(m_dot)/(density*3600*A3n*10^-6);
    D3n=r3n+(2.2-((2.2-0.7)*(n/u)));
    L3n=10.575/u;
    Re3n = density*c3n*D3n*10^-3/(1.74*10^-5);
    lambda3n = 0.0055*(1+(2*10^4*(epsilon/D3n)+10^6/Re3n)^(1/3));
    AP3n=lambda3n*0.5*density*c3n^2*L3n*10^-5/D3n;
    AP34=AP34+AP3n;
    APtotal_3=APtotal_3+AP3n;
end
Prel_4=Prel_3-AP34;

%section 3.1 to 3.2
%discretize in w sections

APtotal_4=APtotal_3;
AP45=0;
w=1000000;
for t=1:w
    r4t=2-((2-0.56)*(t/w));
    A4t=(pi*r4t^2/2)+(0.7*2*r4t);
    c4t=(m_dot-((t*m_dot)/(w+1)))/(density*3600*A4t*10^-6);
    D4t=r4t+0.7;
    L4t=12.98*2*pi*13/61/w;
    Re4t = density*c4t*D4t*10^-3/(1.74*10^-5);
    lambda4t = 0.3164/(0.95*Re4t^0.25)+0.0075*sqrt(D4t/2/(r4t));
    AP4t=lambda4t*0.5*density*c4t^2*L4t*10^-5/D4t;
    AP45=AP45+AP4t;
    APtotal_4=APtotal_4+AP4t;
end
Prel_5=Prel_4-AP45;

%total pressure loss from inlet to volute outlet (1 to 4)
Total_pressure_loss_inlet=APtotal_4;
```

C.2. VOLUTE OUTLET VELOCITY ANGLE

```
%to calculate the angle between the velocity and the normal vector to the
volute outlet surface

epsilon = 13/61; %admission ratio
r_1 = 12.775; %radius of the volute outlet surface
r_2 = 2; %radius of the volute area at the volute inlet
b = 0.7; %width of the volute area
```

```
r_0 = 12.975+2; %distace from turbine centre to volute inlet centre
A_1 = epsilon * pi * 2 * r_1 * b; %volute outlet area
A_0 = 0.5 * pi * r_2^2 + 2 * r_2 * b; %volute inlet area
alpha = atan((r_0/r_1)*(A_1/A_0))*180/pi; %angle between velocity and the
normal vector at the volute outlet
```

C.3. VOLUTE OUTLET PRESSURE LOSS

```
clear
clc %inputs: m_dot, Ra (Roughness)

m_dot=2.859; %input
Ra=3.172; %input
epsilon=Ra*10^-3*11.03;
R=286.9;
density=0.8; %(kg/m^3)

%calculations
%section 1 to 2
r12_1=4; %(mm)
r12_2=1.135; %(mm)
A12=pi*r12_1^2-pi*r12_2^2; %(mm^2)
c12=m_dot/(density*3600*A12*10^-6); %(m/s)
Dh12=2*r12_1-2*r12_2; %(mm)
r12=Dh12/2;
L12=4.7; %(mm)

%moody
Re12 = (density*c12*Dh12*10^-3)/(1.74*10^-5);
lambda12 = 0.0055*(1+(2*10^4*(epsilon/Dh12)+10^6/Re12)^(1/3));
AP12=lambda12*0.5*density*c12^2*L12*10^-5/Dh12;
APtotal_1=AP12; %bar

%section 2 to 3
r23=4; %(mm)
A23=pi*r23^2; %(mm^2)
c23=m_dot/(density*3600*A23*10^-6); %(m/s)
D23=2*r23; %(mm)
L23=4.3; %(mm)

%moody
Re23 = density*c23*D23*10^-3/(1.74*10^-5);
lambda23 = 0.0055*(1+(2*10^4*(epsilon/D23)+10^6/Re23)^(1/3));
AP23=lambda23*0.5*density*c23^2*L23*10^-5/D23;
APtotal_2=APtotal_1+AP23; %bar

%section 3 to 4
%discretize in t sections
APtotal_3=APtotal_2;
t=1000000;
for i=1:t
    r3i=r23+(2*(i/t));
```

```
    A3i=pi*r3i^2;
    c3i=m_dot/(density*3600*A3i*10^-6);
    D3i=r3i*2;
    L3i=20.8/t;
    Re3i = density*c3i*D3i*10^-3/(1.74*10^-5);
    lambda3i = 0.0055*(1+(2*10^4*(epsilon/D3i)+10^6/Re3i)^(1/3));
    AP3i=lambda3i*0.5*density*c3i^2*L3i*10^-5/D3i;
    APtotal_3=APtotal_3+AP3i; %bar
end

%section 4 to 5
r45=6; %(mm)
A45=pi*r45^2; %(mm^2)
c45=m_dot/(density*3600*A45*10^-6); %(m/s)
D45=2*r45; %(mm)
L45=126.2; %(mm)

%moody
Re45 = density*c45*D45*10^-3/(1.74*10^-5);
lambda45 = 0.0055*(1+(2*10^4*(epsilon/D45)+10^6/Re45)^(1/3));
AP45=lambda45*0.5*density*c45^2*L45*10^-5/D45;
APtotal_4=APtotal_3+AP45; %bar

%section 5 to 6
%discretize in t pieces

APtotal_5=APtotal_4;
for n=1:t
    r5n=6-(n/t);
    A5n=pi*r5n^2;
    c5n=(m_dot)/(density*3600*A5n*10^-6);
    D5n=r5n*2;
    L5n=11.4/t;
    Re5n = density*c5n*D5n*10^-3/(1.74*10^-5);
    lambda5n = 0.0055*(1+(2*10^4*(epsilon/D5n)+10^6/Re5n)^(1/3));
    AP5n=lambda5n*0.5*density*c5n^2*L5n*10^-5/D5n;
    APtotal_5=APtotal_5+AP5n; %bar
end

%section 6 to 7

r67=5; %(mm)
A67=pi*r67^2; %(mm^2)
c67=m_dot/(density*3600*A67*10^-6); %(m/s)
D67=2*r67; %(mm)
L67=188.6; %(mm)
%moody
Re67 = density*c67*D67*10^-3/(1.74*10^-5);
lambda67 = 0.0055*(1+(2*10^4*(epsilon/D67)+10^6/Re67)^(1/3));
AP67=lambda67*0.5*density*c67^2*L67*10^-5/D67;
APtotal_6=APtotal_5+AP67; %bar

%Sudden expansion loss section 9
A_1=pi*(0.004^2-0.0028^2)*0.33;
A_2=pi*0.004^2;
c_1=m_dot/(3600*A_1*density);
```

```
sudden_loss_9=density*(A_1/A_2)*(1-(A_1/A_2))*c_1^2/100; %mbar

%Sudden expansion loss section 12
A12=A67;
c_12=m_dot/(density*3600*A12*10^-6);
sudden_loss_12=(1/2)*density*c_12^2/100;


Outlet_loss=sudden_loss_9+(APtotal_6*10^3)+sudden_loss_12; %mbar
```

C.4. TURBINE POWER AND EFFICIENCY

```
%Implement Refprop
addpath('C:\Program Files (x86)\REFPROP\refprop-extras\MATLAB');
addpath(genpath('C:\Program Files (x86)\REFPROP\refprop-
extras\MATLAB\extras-matlab-functions'));

m_dot_exp=2.859; %mass flow (kg/h)
P_in=2.7347; %pressure inlet (bar)
P_out=0.965+0.267465; %pressure outlet (bar)
T_in=220.31+273.15; %temperature inlet (K)
T_out=193.1+273.15; %temperature outlet
density=refpropm('D','T',(T_in+T_out)/2,'P',(P_in+P_out)/2*100,'nitroge
n','oxygen','argon',[0.755 0.231 0.014]);
Cp=refpropm('C','T',(T_in+T_out)/2,'P',(P_in+P_out)/2*100,'nitrogen','o
xygen','argon',[0.755 0.231 0.014]);
R=287.13; %constant gases
density_in=P_in*10^5/(R*T_in); %density inlet (kg/m^3)
density_out=P_out*10^5/(R*T_out); %density outlet (kg/m^3)
K=refpropm('K','T',(T_in+T_out)/2,'P',(P_in+P_out)/2*100,'nitrogen','ox
ygen','argon',[0.755 0.231 0.014]);
Cs=refpropm('A','T',(T_in),'P',(P_in)*100,'nitrogen','oxygen','argon',[
0.755 0.231 0.014]);


%geometry data
c6=Cs; %(m/s)
r6=7.65*10^-3; %(m)
alpha6=22; %stator outlet blade angle (°)
betha7=36.59; %rotor inlet blade angle (°)
r7=7.5*10^-3; %(m)
betha8=138.19; %rotor TE blade angle (°)
r8=6.5*10^-3; %(m)
d8=0.695; %distance between blades (measured with Catia)
h8=0.586; %blade height
A8=d8*h8*13; %area between the blades at the TE
w=168200*pi/30; %(rad/s)

%Mach = 1 in the critical section (stator outlet)

%calculations
Cu6=c6*cos(alpha6*pi/180); %(m/s)
```

```
Cu7=(Cu6*r6)/r7; %(m/s)
u7=w*r7; %(m/s)
Cm8=m_dot_exp/(3600*density_out*A8*10^-6); %perpendicular velocity to A8
W8=Cm8/sin((180-betha8)*pi/180); %relative velocity (m/s)
Wu8=W8*cos((180-betha8)*pi/180); %(m/s)
u8=w*r8; %(m/s)
Cu8=Wu8-u8; %(m/s)
P_exp=m_dot_exp*(Cu7*u7-Cu8*u8)/3600; %turbine power

P_corrected=39.9; %(W) (adding the bearing heat losses)
T_out_corrected=T_in-(P_corrected/((m_dot_exp/3600)*Cp));
P_temperatures=m_dot_exp/3600*Cp*(T_in-T_out);      %turbine      power
experimental
c8=sqrt(Cu8^2+Cm8^2);
Static_pressure_out = P_out -(0.5*density_out*c8^2)*10^-5;
Efficiency_corrected          =          (T_in-T_out_corrected)/(T_in*(1-
((Static_pressure_out/P_in)^((K-1)/K))));
Efficiency_non_corrected            =            (T_in-T_out)/(T_in*(1-
((Static_pressure_out/P_in)^((K-1)/K))));
```

BIBLIOGRAPHY

[1] P. H. Wagner, Integrated Design, Optimization, and Experimental Testing of the World's Smallest Steam-Driven Recirculation Fan for Solid Oxide Fuel Cell Systems, Neuchâtel: EPFL, 2018.

[2] R. I. Lewis, Turbomachinery Performance Analysis, London, 1996.

[3] L. F. Moody, An Appropriate Formula for Pipe Friction Factors, 1947.

[4] P. M. a. S. N. Gupta, Momentum Transfer in Curved Pipes, 1979.

[5] C. G. H. W. Thomas Adams, A Simple Algorithm to Relate Measured Surface Roughness to Equivalent Sand-grain Roughness, USA: Avestia Publishing, 2012.

[6] H. Chanson, The Hydraulics of Open Channel Flow: An Introduction, 1999.

[7] I. ANSYS, ANSYS ICEM CFD 11.0, USA, 2007.

[8] I. ANSYS, Ansys CFX Tutorials, USA, 2010.

[9] S. L. Dixon, Fluid Mechanics and Thermodynamics of Turbomachinery, UK: Elsevier Inc., 2014.

[10] S. A. Korpela, Principles of Turbomachinery, USA: John Wiley and Sons, Inc., 2011.